A Study on Connectome-based Neural Network Models of Motion Generation in *Caenorhabditis elegans*

(コネクトームに基づく線虫の運動生成神経回路モデルに関する研究)

By

Kazuma Sakamoto

Graduate School of Advanced Science and Engineering

Hiroshima University

November 2021

Contents

List of Figures

Chapter 1

1 Introduction

1.1 Background and Purpose

Caenorhabditis elegans (*C. elegans*) is a multicellular organism with a length and weight of approximately 1.0 mm and 0.5 μg, respectively. This organism's body and nervous system comprise approximately 1,000 cells and 302 neurons, respectively [1]. Despite such a small number of neurons, information processing flow in this organism occurs in a manner similar to that in higher organisms that sense environmental information and control muscles to perform appropriate movements. Therefore, this organism has been used herein to investigate the mechanisms of motion pattern generation and information processing. The connection structure of the *C. elegans* neural network has already been clarified, and in recent years, the function of each neuron has been clarified by imaging technology using fluorescent proteins and electrophysiological measurement technology. However, it is difficult to elucidate the information processing mechanism of the neural network using only a bottom-up experimental approach. Therefore, a top-down approach using a mathematical model has been adopted. However, these models don’t base on the actual connection structure of *C. elegans*. To make a model by the simplifying connection structure may lead to an incorrect interpretation of the information mechanism.

In this study, we construct a neural network model that preserves the actual neural network structure

and adjust the parameters using a learning algorithm called Backpropagation through time (BPTT) to simulate the internal representation of the chemical concentration gradient and the generation of forward and backward motion. Then, we clarify the function and feature of the neural circuit of *C. elegans* that contributes to information processing of chemotaxis and motion generation.

1.2 Related Works

1.2.1 Chemotaxis model and Simulation

Chemotaxis is one of the fundamental abilities of sensing chemical information and approaching a favourable environment based on the sensory information. *C. elegans* employs two types of behavioural strategies to perform chemotaxis. Pirouette is a strategy characterised by a series of behaviours starting with backward movement followed by sharp turns to change the travelling direction, and its occurrence depends on the chemical gradient parallel to the travelling direction of the body[2]. Weathervane represents a strategy of making a gradual curve toward a chemical peak, where the curving rate depends on the chemical gradient perpendicular to the travelling direction of the body[3]. If multiple sensory neurons are located spatially apart from each other, the gradients could be internally represented by the difference between their responses. However, the sensory neurons, for example, ASEL and ASER in the case of salt chemotaxis, are located in close proximity at the nose tip. Therefore, the neural network is required to calculate and internally represent two types of

gradients using the temporal responses of the sensory neurons.

The input to a pair of interneurons (AIYL and AIYR) may play this role, as suggested by a study by Kocabas *et al*.[4], which found that the symmetric input to the neurons changes the frequency of pirouette and that the asymmetric input controls the curving rate. In addition, model studies have predicted neural processing related to the weathervane strategy. Ferrée *et al*.[5] constructed a simple nonlinear neural-network model to enable weathervane, and also extracted its computational rules using the impulse response of a linear neural network[6]. Morse *et al*.[7] then verified the neural network model by navigating a robot to a light source. Izquierdo and Lockery[8] subsequently proposed a simplified network structure that could adjust the curving rate from sensory inputs, and found that the nonlinearity and self-feedback of motor neurons may serve as key mechanisms for this function. Furthermore, their group demonstrated that the neural network model derived from the connectome was also able to perform weathervane[9]. Xu *et al*.[32] proposed a dynamic neural-network model and simulated attraction and avoidance behaviour; in addition, their group recently combined a body dynamics model and a neural network model to enable chemotaxis[10].

An understanding of chemotaxis acquired from the previous studies can be interpreted from the viewpoint of Marr's level of analysis[33]. The behavioural analysis[2,3] highlighted the problem at the computational level that the chemotaxis is closely related to the chemical gradients in the environments. The neural activity measurements[4] revealed the phenomena at the implementational

level. The simulation approaches[5-10] analysed the information-processing mechanism at the algorithmic and implementational levels. However, these approaches did not directly treat the algorithm to calculate chemical gradients in the environments, which was explicitly or implicitly assumed given in the computational level. In other words, the relationships between the sensory input at the nose tip of *C. elegans* and internal representations of the two types of chemical gradients in the environments closely related to the observed strategies have not been formulated explicitly. Therefore, a gap exists between computational and implementational levels. Further, most previous models focused on revealing the mechanism of the weathervane and did not simulate the pirouette simultaneously.

This dissertation presents a simple and comprehensive computational model based on the motion of the animal involved in chemotaxis to bridge the gap of understanding between computational and implementational levels. The ability of the computational model to convert sensory inputs at the nose tip of *C. elegans* into internal representations of the chemical gradient parallel and perpendicular to the travelling direction was verified using a chemotaxis simulator that can simulate the body motions of pirouette and weathervane. The chemotaxis performance of the model was compared with previous experimental data[3]. For additional analysis of the implementational level, a connectome-based neural network model was constructed to test whether the computation could be implemented. Based on these results, we also discuss the relationship between the proposed

computational model and the findings of the experimental[4] and model[9] studies.

1.2.2 Muscle Activity Generation Model and Simulation

C. elegans produces various movement patterns by adjusting its whole-body movement according to diverse environmental stimuli [1–4]. Thus, the worm is a suitable model animal for investigating the mechanism of motion pattern generation.

The neural circuit structure related to motion generation has been clarified to some extent by biological experiments. Chalfie *et al*. revealed the role of interneurons that control forward and backward movement through experiments involving laser irradiation [1]. The anatomical study carried out by White *et al*. successfully mapped the connectome of *C. elegans* [5], and updated data can be accessed through the web database WormAtlas [6]. Figure 1 shows the neuromuscular connectome related to movement based on the Connectome database (accessible at https://wormwiring.org/series/). Further experimental studies revealed the functions of the neural circuit structure. For example, Wen *et al*. [7] found that proprioceptive feedback is essential for motion generation, and Kawano *et al*. [8] showed that gap junctions are important for motion generation.

Although the structure and role of neurons related to movement have been clarified by experimental methods, explicating the function of the neural circuit requires the measurement and interpretation of the activity of each neuron. However, performing these tasks using only a bottom-up

experimental approach would be extremely difficult. Therefore, a top-down approach using a mathematical model has been employed. Niebur and Erdös constructed a body dynamics model incorporating the central pattern generator to analyze the forward movement of *C. elegans* [9], and postulated that stretch receptors are important for the generation of movement. Bryden and Cohen analyzed the gait generation mechanism of forward movement using a body model incorporating the command neuron AVB and motor neurons [10]. An integrated neuromechanical model proposed by Cohen's group [10–12] is often used in recent research to study neuromuscular control. Olivares *et al*. [13] presented a model that incorporates the connectome and verified the existence of both a central pattern generator in the ventral nerve cord and the role of command neurons in switching between forward and backward motion. Fieseler *et al*. [14] found that suppression of proprioceptive feedback may contribute to the generation of an omega turn. Although various aspects of motion generation in *C. elegans* have been elucidated, these models assigned the same values to the same types of connection parameters, which is unrealistic because the synaptic strength follows a modified Boltzmann distribution according to observation in the actual animal [15]. This modified Boltzmann distribution indicates that the network is sparsely connected, consisting of a large number of weak connections and a small number of strong connections.

In this study, we examined whether the motor neuron and muscle network could generate oscillation patterns for both forward and backward movement without imposing the unrealistic

constraints for the strengths of synaptic and gap connections. The proposed model consists of command neurons that control forward and backward movement and motor neurons of classes A, B, D, AS, and muscle. Both gap junctions and synaptic connections are included based on the connectome data. We assumed on/off outputs of the command neurons based on their role in evoking forward and backward movements [1,8], and generated teacher data from measured muscle activities of a strain expressing calcium indicator in the body-wall muscle (HRB4). The connection parameters were then trained using a supervised algorithm. Finally, the trained model was driven by the untrained input of the command neuron to examine its generalizability, and the fit of trained weights to the modified Boltzmann distribution was tested.

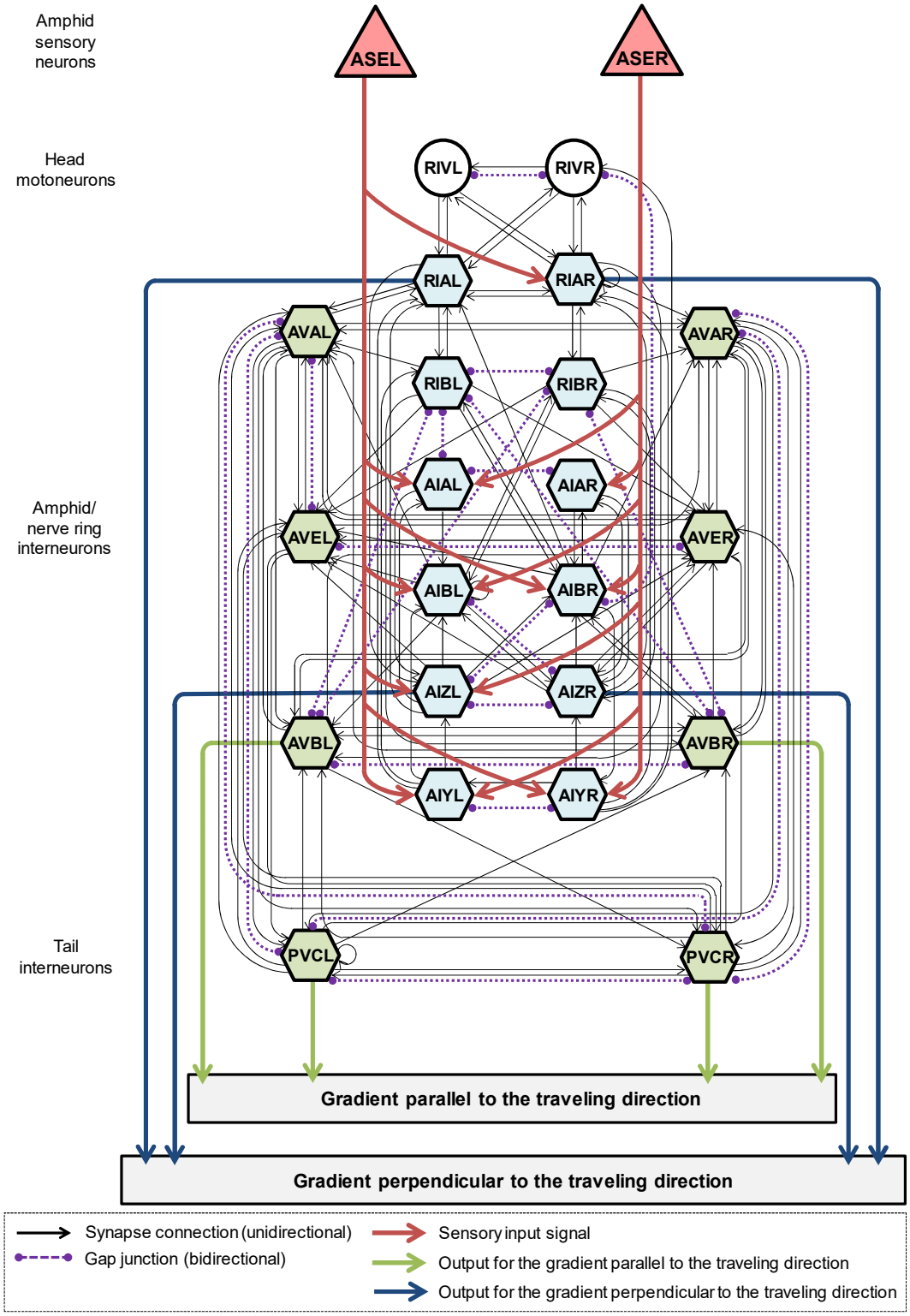

Figure 1. Structure of the neural network model regarding to chemotaxis in *C. elegans*.

1.3 Content Outline

The dissertation is organized as follows:

Chapter 2 describes the neural network model of *C. elegans.* This model is composed with integrate-and-fire neuron model which the membrane potential rises sharply when the time integration of the input signal exceeds the threshold value. Imitating the information transmission method of nerve cells in an actual organism, input to each neuron is composed with term which represent information transmission by synaptic connection and term which represent information transmission by electrical connection, and neurons are connected based on construct which is clarified by biologically. The strength of the connection is optimized using Backpropagation through time (BPTT), which is a learning algorithm for recurrent neural nets.

In Chapter 3, we propose the computational model that generates an internal representation of the chemical concentration gradient which is guessed to be used when *C. elegans* chemotaxis, and simulate this internal representation using the model which proposed in chapter2. Computational model shows that bending angle of *C. elegans* head is needed to generate two types of internal representation of chemical concentration gradient which involve in chemotaxis, in addition to the chemical concentration sensed by the *C. elegans* head. As a result of inputting chemical concentration and bending angle of head to neural network model and learning the parameters, it is shown that it can implement computational model to connectome model of *C. elegans*. From the results, it was

suggested *C. elegans* calculates the chemical concentration gradient by integrating the chemical concentration information which is obtained by shaking the head from side to side and decomposing it into a chemical concentration gradient in the direction of movement and the direction of orthogonal. Furthermore, we performed a simulation of destroying the nerve cells of the model and compared it with the results of biological experiments. From the above, it was suggested that the constructed model may be able to predict the results of biological experiments.

In Chapter 4, we focused on the forward and backward movement of *C. elegans*. This model is composed with interneurons, motor neurons, and muscles, and these are connected by connectome. In this simulation, we measured the fluorescence intensity corresponding to muscle activity using transgenic strain of *C. elegans* expressing fluorescent proteins on its body wall muscle, and learning the parameter using this fluorescence intensity as a teacher signal. As a result, it was shown that motor neurons and muscles can generate muscle activity patterns corresponding to forward and backward according to the commands of interneurons. In addition, as a result of analyzing the parameters of the model, trained synaptic weights and conductance weights fitted the modified Boltzmann distribution well. It has been reported that the synaptic connection strength of the real organism also follows the modified Boltzmann distribution, it has been suggested that this model has the features of the neural circuit structure of the real organism. There is no model that has synaptic connection intensity distribution features similar to actual organisms and can reproduce the measured fluorescence intensity.

Therefore, this model may be useful for analysis of the muscle activity generation mechanism.

Chapter 5 describes the summary of this dissertation and future research topics.

Chapter 2

2 Model

2.1 Introduction

This chapter is organized as follows: Section 2.2 outlines the neural network model of *C. elegans*, before Section 2.3 details of the training algorithm.

2.2 Neural Network Model

The neural network model was defined based on the actual connection structure derived from WormAtlas[34] considering both synaptic connections and gap junction. The dynamic characteristic of a neuron is given as follows:

$$x_i(t+1) = \frac{1}{1+T_s\tau_i}x_i(t) + \frac{T_s}{1+T_s\tau_i}\left\{\sum_{j=1}^{n+m} w_{ij}y_j(t) + \sum_{j=1}^{n} g_{ij}\left(x_j(t) - x_i(t)\right)\right\} + \frac{1}{1+T_s\tau_i}\left\{\sum_{j=1}^{n+m} w_{ij}^{d}(y_j(t) - y_j(t-1))\right\}, \quad (1)$$

$$y_i(t) = \frac{1}{1+\exp\left(-x_i(t)\right)}, \quad (2)$$

where $x_i(t+1)$ corresponds to the electrical current to the *i*-th neuron, $y_i(t)$ corresponds to the membrane potential, T_s is the sampling time, τ_i is the time constant caused by leakage current, w_{ij}, and w_{ij}^{d} are the chemical synapse connection strengths from the *j*-th to the *i*-th neuron, $g_{ij} = g_{ji}$ is the conductance of a gap junction, *n* is the total number of neurons, and *m*

is the total input number.

2.3 Training Algorithm

Adjustments of chemical synapse connections w_{ij}, w_{ij}^{d} and gap junctions g_{ij}, and time constant τ_i were performed using back-propagation through a time algorithm, which uses the chain-rule of partial differential on the following evaluation function:

$$E = \frac{1}{T}\frac{1}{n}\sum_{t=1}^{T}\sum_{i=1}^{n}\frac{1}{2}\mu_i\big(d_i(t) - y_i(t)\big)^2, \tag{3}$$

where $\mu_i = 1$ if index i corresponds to the neuron that outputs a gradient either parallel or perpendicular to the traveling direction; otherwise $\mu_i = 0$, $d_i(t)$ is the target gradient that is desired to be outputted from the corresponding neuron, and T is the maximum step number of the simulation time. BPTT updates each parameter in a particular direction to minimize the evaluation function, which is determined by partial differentiation of the evaluation function for the corresponding parameter.

The parameters w_{ij}, w_{ij}^{d}, g_{ij} and τ_i are then iteratively updated based on the partial differential of E by the following equations:

$$w_{ij} \leftarrow w_{ij} - \eta_w \frac{\partial E}{\partial w_{ij}}, \tag{4}$$

$$w_{ij}^{d} \leftarrow w_{ij}^{d} - \eta_{w^d} \frac{\partial E}{\partial w_{ij}^{d}}, \tag{5}$$

$$g_{ij} \leftarrow g_{ij} - \eta_g \left(\frac{\partial E}{\partial g_{ij}} + \frac{\partial E}{\partial g_{ji}}\right), \tag{6}$$

$$\tau_i \leftarrow \begin{cases} \tau_i - \eta_\tau \dfrac{\partial E}{\partial \tau_i} & \tau_i > 0 \\ 0 & \tau_i \le 0 \end{cases}, \tag{7}$$

where $\eta_{w,}\eta_{w^d,}\eta_g,\eta_\tau$ represent the learning rate. As shown in the above equations, the gap junction is constrained to $g_{ij} = g_{ji}$, and the time constant is constrained to $\tau_i > 0$.

The error gradient for w_{ij}, w_{ij}^d, g_{ij} and τ_i are given by the following variation equation each other, and the weights are updated in a batch using.

$$\begin{aligned} \frac{\partial E}{\partial w_{ij}} &= \frac{\partial E}{\partial x_i(t)} \frac{\partial x_i(t)}{\partial w_{ij}} \\ &= \frac{\partial E}{\partial x_i(t)} \frac{T_s}{1 + T_s \tau_i} y_j(t-1), \end{aligned} \tag{8}$$

$$\begin{aligned} \frac{\partial E}{\partial w_{ij}^d} &= \frac{\partial E}{\partial x_i(t)} \frac{\partial x_i(t)}{\partial w_{ij}^d} \\ &= \frac{\partial E}{\partial x_i(t)} \frac{\tau_i}{1 + T_s \tau_i} \{y_j(t-1) - y_j(t-2)\}, \end{aligned} \tag{9}$$

$$\begin{aligned} \frac{\partial E}{\partial g_{ij}} &= \frac{\partial E}{\partial x_i(t)} \frac{\partial x_i(t)}{\partial g_{ij}} \\ &= \frac{\partial E}{\partial x_i(t)} \frac{T_s}{1 + T_s \tau_i} \{x_j(t-1) - x_i(t-1)\}, \end{aligned} \tag{10}$$

$$\frac{\partial E}{\partial \tau_i} = \frac{\partial E}{\partial x_i(t)} \frac{\partial x_i(t)}{\partial \tau_i}$$

$$= \frac{\partial E}{\partial x_i(t)} \left[\frac{T_s}{(1+T_s\tau_i)^2} x_i(t) + \frac{{T_s}^2}{(1+T_s\tau_i)^2} \left\{ \sum_{j=1}^{n+m} w_{ij} y_j(t) \right.\right.$$

$$\left.\left. + \sum_{j=1}^{n} g_{ij} \left(x_j(t) - x_i(t) \right) \right\} + \frac{{T_s}^2}{(1+T_s\tau_i)^2} \left\{ \sum_{j=1}^{n+m} w_{ij}^d \left(y_j(t) - y_j(t-1) \right) \right\} \right], \quad (11)$$

Where error gradient $\frac{\partial E}{\partial x_i(t)}$ is given by the following equation.

$$\frac{\partial E}{\partial x_i(t)} = \mu_i \big(d_i - y_i(t)\big) f'\big(x_i(t)\big) + \sum_{j=1}^{n} \frac{\partial E}{\partial x_j(t+1)} \frac{\partial x_j(t+1)}{\partial x_i(t)} + \sum_{j=1}^{n} \frac{\partial E}{\partial x_j(t+2)} \frac{\partial x_j(t+2)}{\partial x_i(t)}$$

$$= \mu_i \big(d_i - y_i(t)\big) f'\big(x_i(t)\big)$$

$$+ \sum_{j=1}^{n} \frac{\partial E}{\partial x_j(t+1)} \left[\delta_{ij} \frac{1}{1+T_s\tau_j} + \frac{T_s}{1+T_s\tau_j} \left\{ w_{ji} f'\left(x_j(t)\right) + \left(g_{ij} \right.\right.\right.$$

$$\left.\left.\left. - \delta_{ji} \sum_k g_{jk} \right) \right\} + \frac{1}{1+T_s\tau_j} w_{ij}^d f'\left(x_j(t)\right) \right]$$

$$- \frac{\tau_j}{1+T_s\tau_j} \sum_{j=1}^{n} \frac{\partial E}{\partial x_j(t+2)} w_{ji} f'\left(x_j(t)\right), \quad (12)$$

Chapter 3

3 Chemotaxis Model and Simulation

3.1 Introduction

This chapter is organized as follows: Section 3.2 describes the proposed chemotaxis simulator which consist with environmental model, multibody model, and neural network model. Section 3.3 is the result of the simulation and we discuss the result in Section 3.4. Finally, Section 3.5 concludes the chapter.

3.2 Materials and methods

3.2.1 A Simple Computational Model

Behavioural experiments revealed that pirouette and weathervane strategies are closely related to the chemical gradients parallel and perpendicular to the travelling direction[2,3], respectively, but how can these gradients related to the traveling direction be obtained by using only the information accessible by the animal? To answer this question, we focused on the fact that ASEL/R responds to the time derivative of NaCl concentration, and the time derivative can be approximated by a directional derivative (see S2 Appendix 2 for the detailed derivation process). The internal representation of the gradients can then be obtained by decomposing the directional derivative of NaCl concentration sensed at the nose tip into the directional components parallel and perpendicular to the travelling direction.

Based on this idea, a computational model is derived by using the directional derivative and first mean value theorem for definite integrals. The derived computational model is expressed by equations (13) and (14), to describe the relationships between the chemical concentration sensed at the nose tip and the internal representations of the chemical gradient in the environments, respectively.

$$\frac{dy_p}{dt} = -a_p y_p + b_p \frac{dc(\boldsymbol{x_0}, t)}{dt} + \epsilon_p, \tag{13}$$

$$\frac{dy_w}{dt} = \begin{cases} -a_w y_w + b_w \dfrac{dc(\boldsymbol{x_0}, t)}{dt} + \epsilon_w & (q_0 > 0) \\ -a_w y_w - b_w \dfrac{dc(\boldsymbol{x_0}, t)}{dt} + \epsilon_w & (q_0 \leq 0) \end{cases}, \tag{14}$$

where y_p and y_w are the internal representations of the gradients parallel and perpendicular to the travelling direction at the body centre, respectively, and q_0 is the head-bending angle (cf. Materials and Methods; Multibody model); a_p and a_w are the reciprocals of the time constants that smooth the time derivative of the NaCl concentration sensed at the nose tip, and b_p and b_w are the gain constants to scale the inputs. The parameters in the model were adjusted and then set as follows: $a_p = 0.58, a_w = 0.73, b_p = 1.20, b_w = 1.46$. Because the derivation process involves several assumptions and approximations, we use ϵ_p and ϵ_w to express the accumulated approximation errors (see S2 Appendix 2).

The computational model can be interpreted as follows: Equation (13) works as a low-pass filter to eliminate the head-bending component, and equation (14) allows the comparison of the NaCl

concentration between the ventral and dorsal sides using head-bending angles required to calculate the internal representation of the gradient perpendicular to the travelling direction (note that *C. elegans* lies on its side and navigates by dorsoventral motions).

To test the computational model, a chemotaxis simulation involving both weathervane and pirouette strategies was performed by using a multibody model of *C. elegans* and the chemical environmental model.

3.2.2 Neural Network Model

The neural network model shown in Fig. 1 was defined based on the actual connection structure derived from WormAtlas[34] considering both synaptic connections and gap junction, and neurons included in the model were derived from Iino and Yoshida (2009)[3]. The model receives inputs of the head-bending angles and NaCl concentration at the nose tip of the multibody model from RIV(L/R) and amphid sensory neurons ASE(L/R), respectively. The ASEL and ASER responses are determined from the previous experimental data[11] and sent to the interneurons in both amphid and nerve ring. To facilitate the evaluation of implementability of the computational model on the neural network, we assumed that the interneurons could directly generate the gradients, although previous studies[4,8,9] have suggested that these gradients are not directly coded in the *C. elegans* neural network. In this case, PVC(L/R) and AVB(L/R) interneurons were assumed to output the gradient parallel to the

travelling direction because these neurons are responsible for controlling forward motion[12] and may inhibit backward motion followed by a sharp turn. Additionally, interneurons RIA(L/R) and AIZ(L/R) were assumed to output the gradient perpendicular to the travelling direction because these neurons control head bending[35], which can generate turning bias. The following equations give a mathematical definition of the neural network model:

The dynamic characteristic of a neuron is given as follows:

$$u_i(t+1) = \frac{1}{1+T_s\tau_i}u_i(t) + \frac{T_s}{1+T_s\tau_i}\left\{\sum_j^{n+m} w_{ij}z_j(t) + \sum_j^{n} s_{ij}\left(u_j(t)-u_i(t)\right)\right\} + \frac{1}{1+T_s\tau_i}\left\{\sum_j^{n+m} w_{ij}^d\left(z_j(t)-z_j(t-1)\right)\right\}, \quad (15)$$

$$U_i(t+1) = \frac{1}{1+\exp\left(-u_i(t+1)\right)}, \quad (16)$$

where $u_i(t)$ corresponds to the electrical current to the *i*-th neuron, $U_i(t)$ corresponds to the membrane potential, T_s is the sampling time, τ_i is the time constant caused by leakage current, w_{ij}, and w_{ij}^d are the chemical synapse connection strengths from the *j*-th to the *i*-th neuron, $s_{ij} = s_{ji}$ is the conductance of a gap junction, *n* is the total number of neurons, and *m* is the total input number. Additionally, $z_j(t) = u_j(t)$ when $j \le n$, and $z_j(t) = I_{j-n}(t)$ when $n < j \le n+m$ where $I_j(t)$ is the external input including NaCl concentration and head-bending angle $q_0(t)$.

ASER and ASEL neurons were modelled based on the experimental data[11] as follows:

$$I_1(t) = \begin{cases} a_L \log\left(b_L \frac{dc}{dt} + 1\right) & (\frac{dc}{dt} > 0) \\ 0 & (\frac{dc}{dt} \leq 0) \end{cases}, \quad (17)$$

$$I_2(t) = \begin{cases} a_R^+ \log\left(b_R^+ \frac{dc}{dt} + 1\right) & (\frac{dc}{dt} > 0) \\ a_R^- \log\left(b_R^- \frac{dc}{dt} + 1\right) & (\frac{dc}{dt} \leq 0) \end{cases}, \quad (18)$$

where $I_1(t+1)$ and $I_2(t+1)$ represent inputs to ASEL and ASER neurons, respectively. dc/dt is the NaCl concentration time derivative at the nose tip. The parameters $a_L, b_L, a_R^+, b_R^+, a_R^-, b_R^-$ are adjusted to fit the response peaks of ASEL and ASER neurons. Figure 2 shows the fitting results, which confirms that the model could generate a response similar to the experimental data[11].

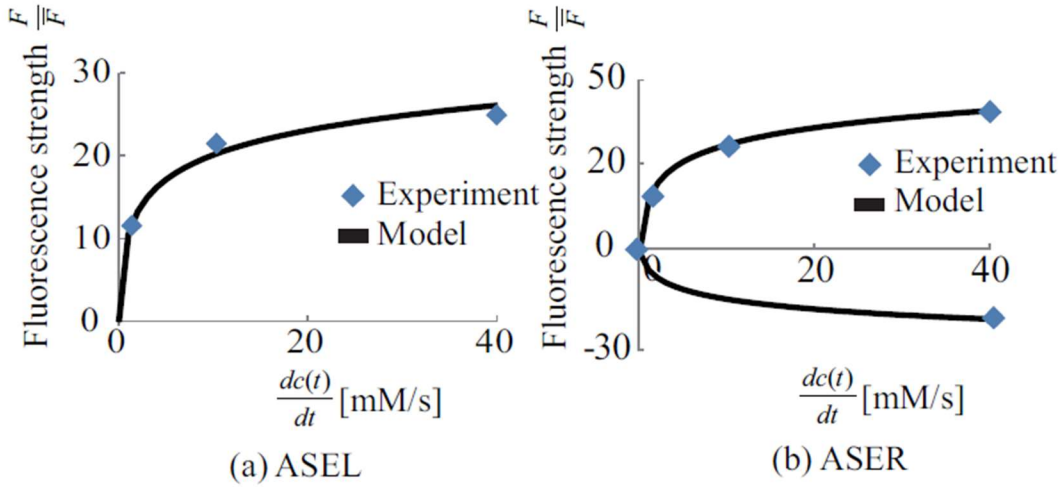

Figure 2. Measured peak responses and the input to the model.

(a) shows the input to ASEL**. (b)** shows the input to ASER**.**

Adjustments of chemical synapse connections w_{ij} and gap junctions s_{ij} were performed using back-propagation through a time algorithm, which uses the chain-rule of partial differential on the following evaluation function:

$$H = \frac{1}{2}\sum_{t=1}^{T}\sum_{i=1}^{n}\mu_i\big(U_i(t) - d_i(t)\big)^2, \tag{19}$$

where $\mu_i = 1$ if index i corresponds to the neuron that outputs a gradient either parallel or perpendicular to the traveling direction; otherwise $\mu_i = 0$, $d_i(t)$ is the target gradient that is desired to be outputted from the corresponding neuron. The chemical gradient is normalised to produce $d_i(t)$ by using the following equations as the output values of a neuron model are in the range of [0, 1].

$$d_i(t) = \frac{c_\zeta(t) - \min\limits_t\left(c_\zeta(t)\right)}{\max\limits_t\left(c_\zeta(t)\right) - \min\limits_t(c_\zeta(t))}, \tag{20}$$

where c_ζ is a gradient either parallel or perpendicular to the traveling direction. The parameters w_{ij}, s_{ij}, τ_i are then iteratively updated based on the partial differential of H by the following equations:

$$w_{ij} \leftarrow w_{ij} - \eta_w \frac{\partial H}{\partial w_{ij}}, \tag{21}$$

$$s_{ij} \leftarrow s_{ij} - \eta_g\left(\frac{\partial H}{\partial s_{ij}} + \frac{\partial H}{\partial s_{ji}}\right), \tag{22}$$

$$\tau_i \leftarrow \begin{cases} \tau_i - \eta_\tau \dfrac{\partial H}{\partial \tau_i}, & \tau_i > 0 \\ 0 & \tau_i \le 0 \end{cases}, \tag{23}$$

where $\eta_{w,}\eta_g, \eta_\tau$ represent the learning rate. As shown in the above equations, the gap junction is constrained to $s_{ij} = s_{ji}$, and the time constant is constrained to $\tau_i > 0$.

3.2.3 Multibody Model

C. elegans body was approximated using a multibody model, as shown in Fig. 3, defined by the following Newton-Euler equations based on a previous study[13]:

$$\boldsymbol{I}(\boldsymbol{q})\frac{d^2\boldsymbol{x}}{dt^2} + \boldsymbol{h}\left(\boldsymbol{q}, \frac{d\boldsymbol{q}}{dt}\right) + \boldsymbol{g}(\boldsymbol{q}) = \boldsymbol{\rho} + \sum_j \boldsymbol{J}_j^T \boldsymbol{F}_j, \tag{24}$$

$$\boldsymbol{I}_g(\boldsymbol{q})\frac{d^2\boldsymbol{x}_g}{dt^2} + \boldsymbol{h}_g\left(\boldsymbol{q}, \frac{d\boldsymbol{q}}{dt}\right) + \boldsymbol{g}_g(\boldsymbol{q}) = \sum_j \boldsymbol{F}_j, \tag{25}$$

where $\boldsymbol{x} = [x_i, y_i]^{\mathbf{T}}$ represents the *i*-th body centroid position, $\boldsymbol{x_g} = [x_g, y_g]^{\mathbf{T}}$ represents the body centre position, $\boldsymbol{q} = [q_0, q_1, \cdots, q_{L-1}]^{\mathrm{T}}$ represents the angles between adjacent modules, $\boldsymbol{I}(\boldsymbol{q})$ and $\boldsymbol{I}_{\mathrm{g}}(\boldsymbol{q})$ represent the inertia matrix, $\boldsymbol{h}\left(\boldsymbol{q}, \frac{d\boldsymbol{q}}{dt}\right)$ and $\boldsymbol{h}_{\mathrm{g}}\left(\boldsymbol{q}, \frac{d\boldsymbol{q}}{dt}\right)$ are centrifugal and Coriolis force terms, $\boldsymbol{g}(\boldsymbol{q})$ and $\boldsymbol{g_g}(\boldsymbol{q})$ are gravity force terms, $\boldsymbol{\rho} = [\rho_0, \rho_1, \cdots, \rho_{L-1}]^{\mathrm{T}}$ is the driving torque generated from the motors, $\boldsymbol{F_j} = [F_{T,j}, F_{N,j}]$ is the friction vector between the floor and the *j*-th body, and $\boldsymbol{J_j}$ is the Jacobian matrix. Please note that we omit the explicit notation of time dependence of the variables for simplification, but all variables depend on time in equations (24) and (25).The parameters related to inertia, centrifugal, Coriolis, and gravity forces are determined based on animal size and weight (Tables in S1 Appendix 1). The friction forces were determined based on the average velocity of the animal on the chemotaxis plate (0.12 mm/s)[3].

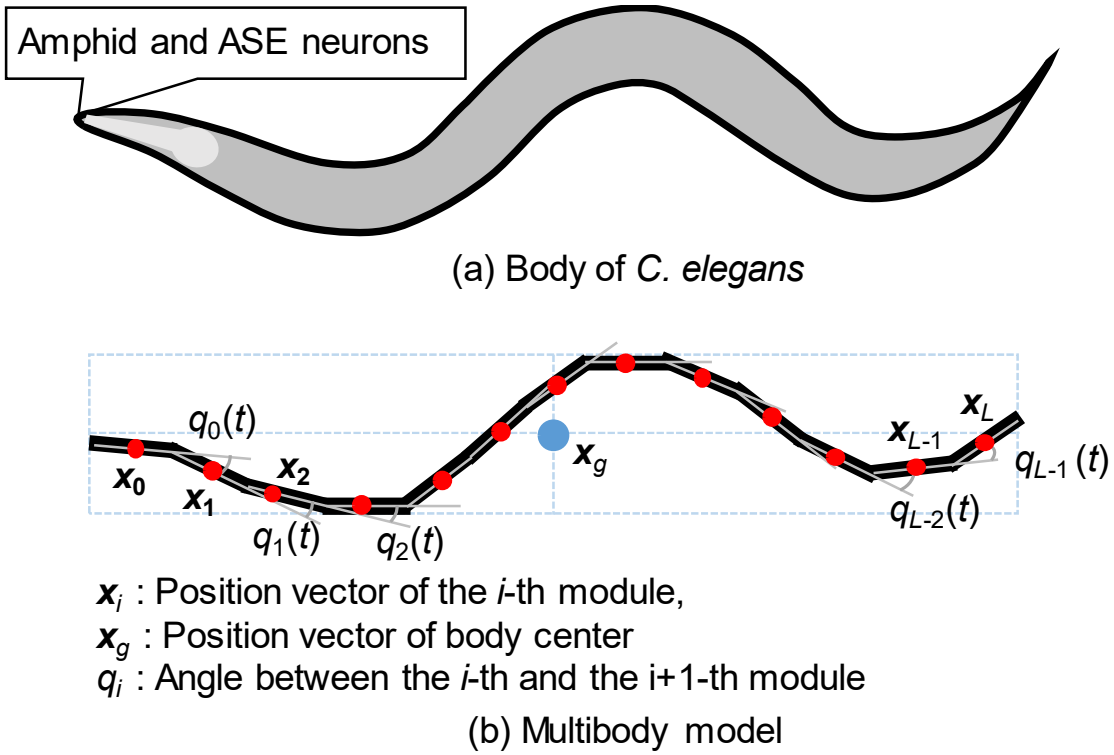

Figure 3. Body of *C. elegans* and the multibody model.

3.2.4 Environmental Model

The environmental model and its parameters were derived from a previous study[3]. NaCl concentration at an arbitrary position $\boldsymbol{x}$ can be calculated by solving Fick's equation as follows:

$$c(x,t) = N_0 \sum_{k=1}^{K} \frac{\exp\left(-\frac{|\boldsymbol{x}-\boldsymbol{x}_k|}{r_1 Dt}\right)}{r_2 EDt} \tag{26}$$

where N_0 is the NaCl solution concentration, D is the NaCl diffusion coefficient, E is the agar plate thickness, and $\boldsymbol{x}_k$ is the coordinate of the k-th NaCl point.

Chemotaxis simulations were performed after 3600 s of NaCl diffusion, with each being performed for 1200 s and repeated 10 times using the multibody model. Notably, NaCl continued to diffuse during the simulation based on equation (26).

3.3 Results

3.3.1 Chemotaxis Simulation using Multibody Model

To evaluate the computational model represented by equations (13) and (14), it is necessary to determine the true chemical concentration at the nose tip and responses of sensory neurons (ASEL and ASER) as well as internal representations of the gradient. However, it is difficult to retrieve this information using experimental approaches. Therefore, we constructed a chemotaxis simulator including a multibody model that can perform motions related to pirouette and weathervane and an environmental model that can simulate the NaCl distribution on the agar plate (cf. Materials and

methods, Chemotaxis simulator). This method enables the verification of the computational model at the behavioural level without measurement of internal representations of the gradients in the actual neural network. Fig. 4(a) shows travelling path examples of the body centre obtained by chemotaxis simulation using the chemotaxis simulator. The chemotaxis simulation was repeated 10 times. In this simulation, the internal representation of the gradients parallel and perpendicular to the travelling direction were calculated using the computational model (equations (13) and (14)), and the calculated values were used to control the motion of the body model to perform pirouette and weathervane. The average travelling speed of the model was 1.28 ± 0.09 mm/s, which is consistent with the experimental data[3]. Figure 4(b) compares the chemotaxis index between the body model and the animals. Based on the previously defined chemotaxis index[3], it is calculated as $(T_{in}-T_{out})/T_{total}$, where T_{in} is the time spent within $\sqrt{(2/\pi)}$ cm from any NaCl peak, T_{out} is time spent outside the area, and T_{total} is the total simulation and experiment time, which is 1200 s in this case. The figure confirms a chemotaxis index of 0.64 ± 1.38 for the simulation. A comparison between the multibody model and the animal is presented in S3 Supplemental information from the following aspects: the pirouette motion of the multibody model, a relationship between the curving rate and the gradient perpendicular to the traveling direction, a relationship between the bearing angles and the sharp turn angle, and evaluation of the error caused by converting body postures into the travelling path by using the multibody model.

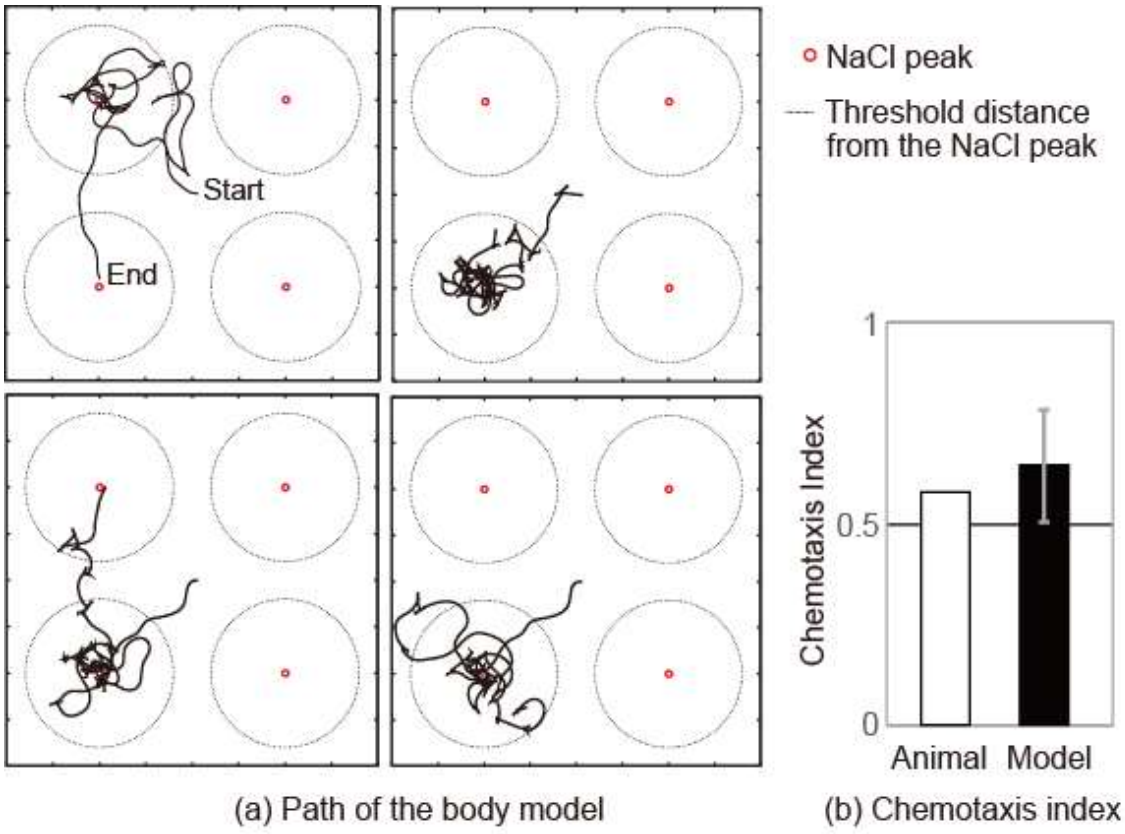

Figure 4. Chemotaxis simulation using the multibody model.

(**a**) Schematic of four examples of chemotaxis paths out of 10 simulations. The body model was placed at the centre of the field and chemotaxis simulation was performed for 1200 s. The resultant paths of the body centre are shown as solid dark lines. The small red circles with the solid line indicate the NaCl peaks and the circles with the broken line indicate the threshold distance used to calculate the chemotaxis index[3]. (**b**) Chemotaxis indices of the simulation and the animal. The error bar represents the standard deviation of 10 simulations.

The true values of the gradients parallel and perpendicular to the travelling direction, denoted as y_p^G and y_w^G, respectively, were then geometrically calculated based on the chemotaxis simulation path of the body centre, as described in Materials and Methods (Geometrical calculations of NaCl gradient), and compared with the internal representation of the gradients calculated using the computational model (equations (13) and (14)). Figure 5 shows comparison examples. The figure confirms a high correlation of $r = 0.91$ ($p < 0.01$) and $r = 0.89$ ($p < 0.01$) for the gradients parallel and perpendicular to the travelling direction, respectively. The average correlations over 10 chemotaxis simulations were $r = 0.90 \pm 0.03$ and $r = 0.91 \pm 0.02$, and the average root mean square error (RMSE) values were $1.71 \pm 0.32 \times 10^{-6}$ mM/s and $0.14 \pm 0.01 \times 10^{-3}$ mM/cm, for the respective gradients.

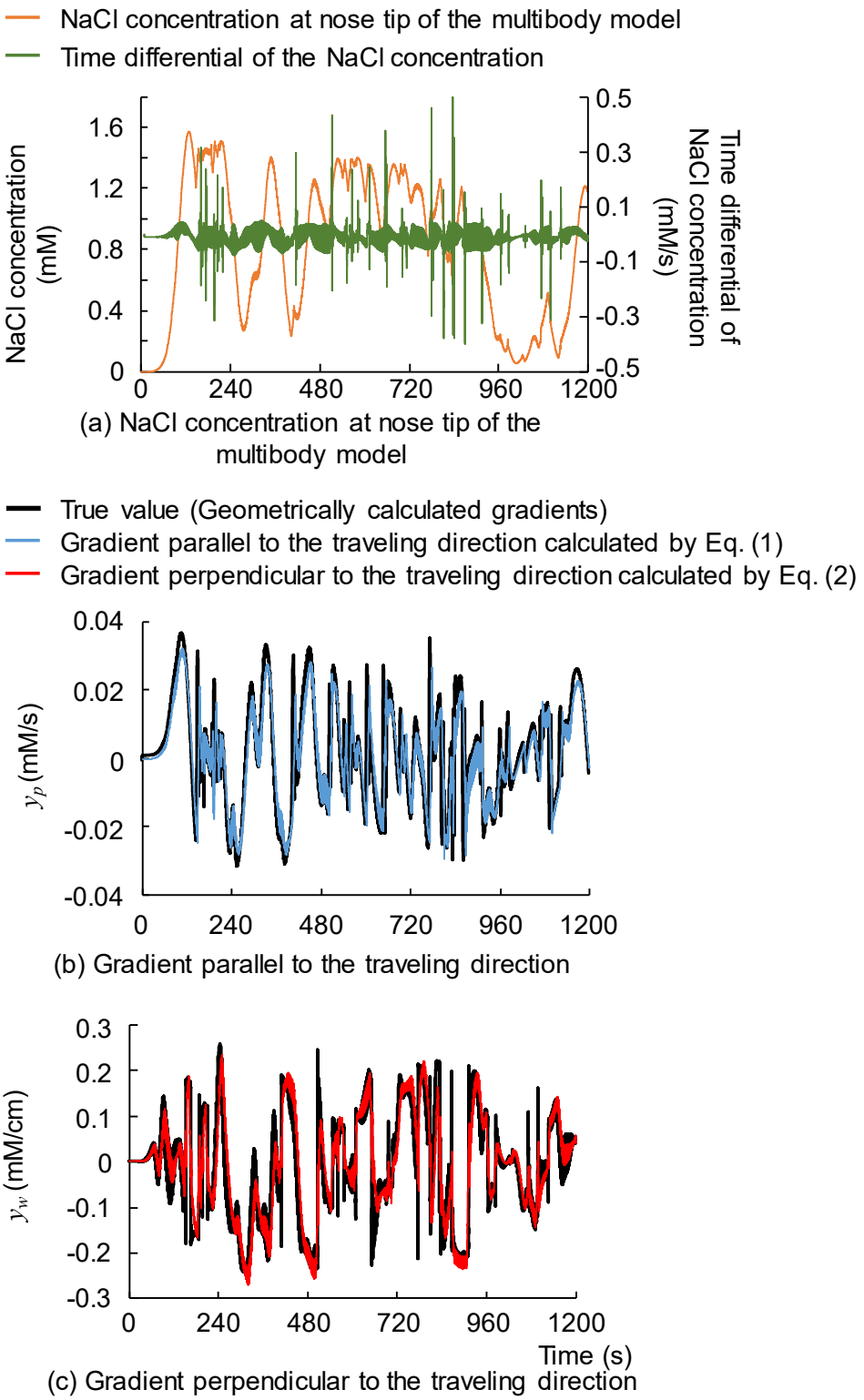

Figure 5. Comparison of the internal representation of the gradients generated by the computational model and geometrically calculated gradient (true value).

Black lines indicate the true gradients geometrically calculated from the chemotaxis path shown in the

upper left side of Fig. 4.

(a) NaCl concentrations at the nose tip of the multibody model and time differential of the concentration corresponding to dc/dt in equations (13) and (14). Spikes observed in the time differential of the NaCl concentration are caused by backward movement for the initiation of pirouette.

(b) Comparison of the gradient parallel to the travelling direction. The correlation is $r = 0.91$ ($p < 0.01$) and RMSE is 1.78×10^{-6} mM/s.

(c) Comparison of the gradient perpendicular to the travelling direction. The correlation is $r = 0.89$ ($p < 0.01$) and RMSE is 0.15×10^{-3} mM/cm.

The computational model was derived based on several assumptions and approximations regarding the inputs. We thus tested input $(q_0, dc(\boldsymbol{x}_0, t)/dt)$ dependency of the errors, as shown in Fig. 6. Here, the errors are defined as $e_p = y_p^G - y_p$ and $e_w = y_w^G - y_w$, respectively, for the gradient parallel and perpendicular to the travelling direction. The figure confirms low correlations between the inputs and the errors. The average correlations of the 10 simulation results are as follows:

q_0 vs e_p: 0.01± 0.02

$dc(\boldsymbol{x}_0, t)/dt$ vs e_p: 0.08± 0.05

q_0 vs e_w: 0.01± 0.02

$dc(\boldsymbol{x}_0, t)/dt$ vs e_w: 0.1± 0.06

*$p < 0.001$ for all correlations

These results demonstrate low correlations between the errors and inputs, indicating almost no input dependency.

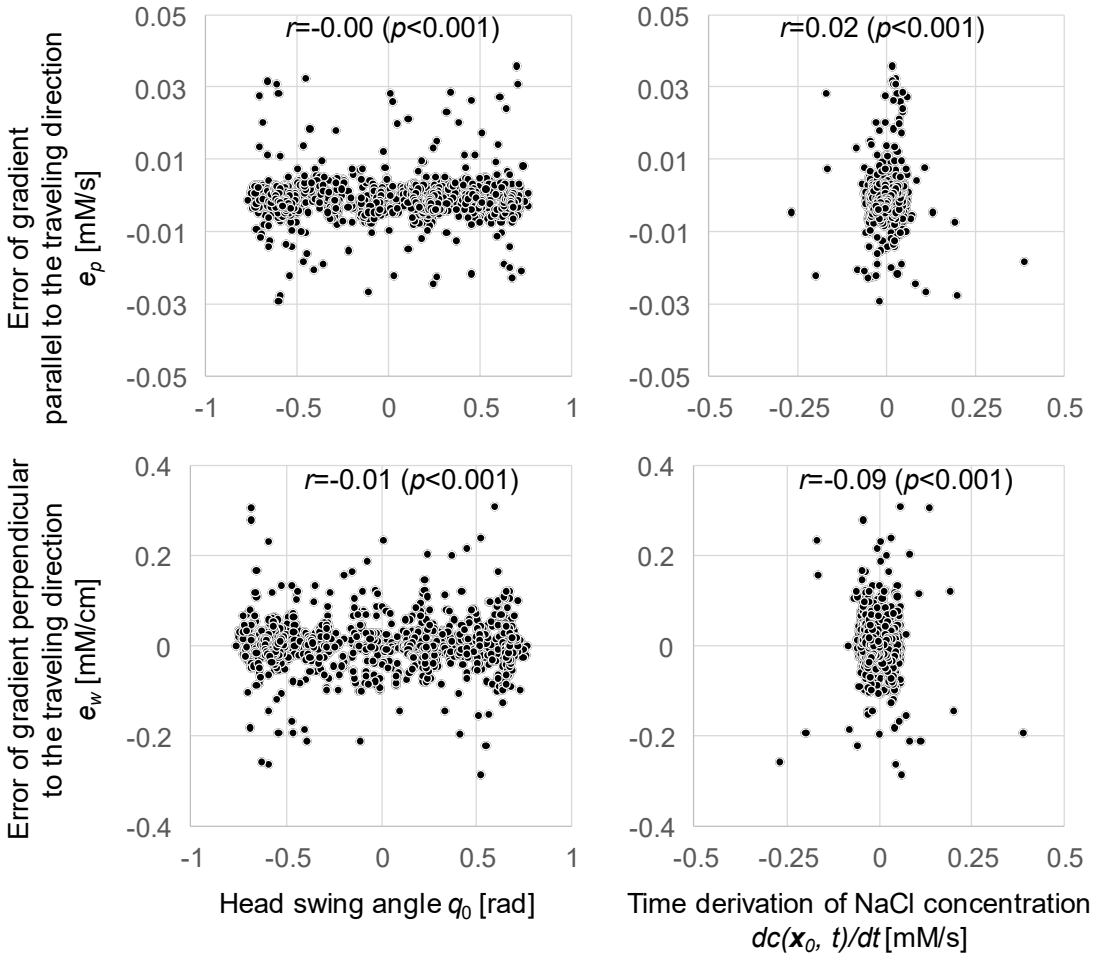

Figure 6. Input dependency of error in gradients parallel and perpendicular to the traveling direction.

Errors between the gradients calculated geometrically and those generated by the computational model are plotted against the inputs to the computational model. The errors and inputs are obtained from the chemotaxis simulation results shown in the upper left part of Fig. 4(a).

3.3.2 Generating Internal Representations of Chemical Gradient using Neural Network Model

The computational model indicates that generating the internal representation of NaCl gradients requires the time derivative of NaCl concentration at the nose tip and head-bending angle. We thus tested whether the connectome-based neural network exhibited the ability to generate the internal representations from this information. A neural network model was constructed based on the neural connection structure derived from WormAtlas[34] and neurons included in the model were chosen based on those treated in Iino and Yoshida (2009)[3]. The simulation results were then compared with the computational model described by equations (13) and (14). The structure of the network model is shown in Fig. 1.

The model considers the response characteristics of sensory neurons ASEL and ASER using equations (17)–(18) (cf. Materials and Methods, Neural network model) based on measured data[11]. In addition, although previous studies[2,4,5] suggested that the gradients are not directly coded in the neural network of *C. elegans*, to facilitate the evaluation of the implementability of the computational model in the neural network, we assumed that the interneurons explicitly represent these gradients. In this case, PVC(L/R) and AVB(L/R) interneurons were assumed to output the gradient parallel to the travelling direction because these neurons are responsible for controlling forward motion[12] and may inhibit backward motion followed by a sharp turn. In addition, the RIA(L/R) and AIZ(L/R)

interneurons were assumed to output the gradient parallel to the travelling direction because these neurons control head bending[36,14], which can generate turning bias. The model considers both chemical synapse connections and gap junctions; these connection weight parameters were trained using back-propagation through a time algorithm[15] modified to simultaneously train the parameters of both gap junctions and chemical synapses. The training datasets were generated using data from the chemotaxis simulation performed using the multibody model, wherein the inputs were the NaCl concentration sensed at the nose tip of the multibody model and the head-bending angles, and the teacher signals comprised true chemical gradients that were geometrically calculated from the path of the body centre obtained from the chemotaxis simulation.

Figure 8a and b show an example of comparison results between the output of the trained neural network model and the true chemical gradients, where the data in the time interval of 0–300 s are used for training the neural network and the data in the remaining 300 s are used to validate generality. The result confirmed the correlations of $r = 0.94$ ($p < 0.01$) and $r = 0.99$ ($p < 0.01$) for the gradients parallel and perpendicular to the travelling direction in the training interval, and $r = 0.92$ ($p < 0.01$) and $r = 0.95$ ($p < 0.01$) for the gradients parallel and perpendicular to the travelling direction in the validation interval, respectively. The average correlations over 10 chemotaxis simulation datasets were $r = 0.91 \pm 0.04$ and $r = 0.97 \pm 0.03$ for the gradients parallel and perpendicular to the travelling direction in the training interval, and $r = 0.89 \pm 0.04$ and $r = 0.91 \pm 0.03$ for the gradients parallel and perpendicular

to the travelling direction in the validation interval, respectively. It should be noted that the gradients were normalised to a range of [−0.5, 0.5] considering the output range of the sigmoid function used in the neural network model.

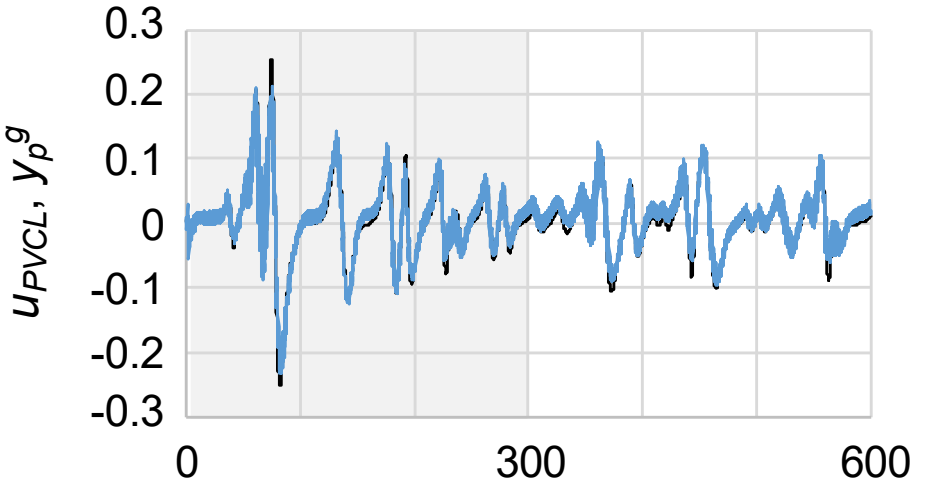

(a) Gradient parallel to the traveling direction

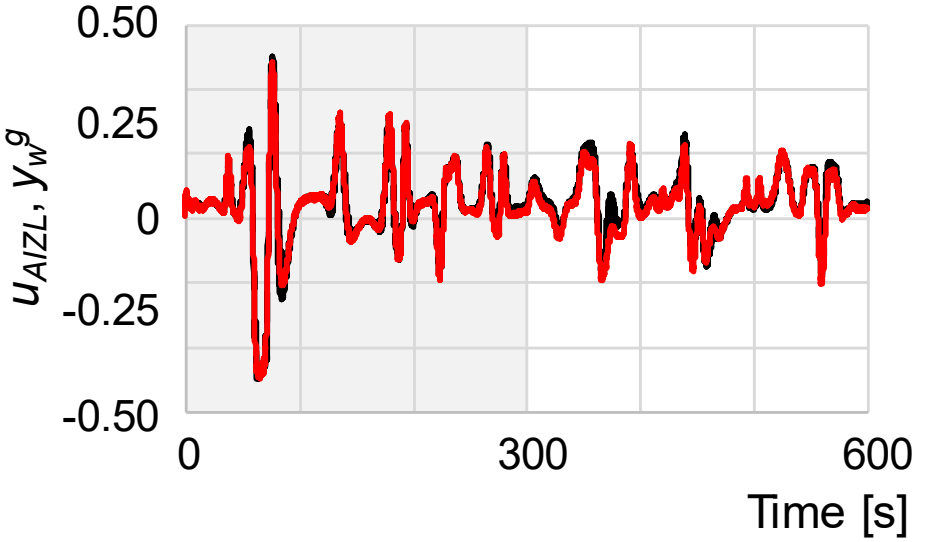

(b) Gradient perpendiculr to the traveling direction

Figure 7. Comparison between the outputs of the connectome-based neural network (coloured lines) and true values of gradients (black lines).

The y-axis shows the NaCl gradient normalised to a range of [−0.5, 0.5] and the x-axis represents time in seconds. The grey highlights indicate the time interval (from 0 to 300 s) used as training data, and the remaining intervals are for validation.

(**a**) Comparison of the output of PVCL and the gradient parallel to the travelling direction. (**b**) Comparison of the output of AIZL and the gradient perpendicular to the travelling direction.

Finally, we compared the computational model with the neural network model. For this comparison, the outputs of the computational model (equations (13) and (14)) were calculated for the 10 chemotaxis-simulation datasets using the previously described parameters. Figure 9(a) and (b) show examples of the outputs of the neural-network model and the computational model. Figure 9(c) shows the correlations between the outputs of the neural network model and those of the computational model where the average correlations were $r = 0.93 \pm 0.04$ for both gradients parallel and perpendicular to the travelling direction and $p < 0.01$ for all simulation datasets.

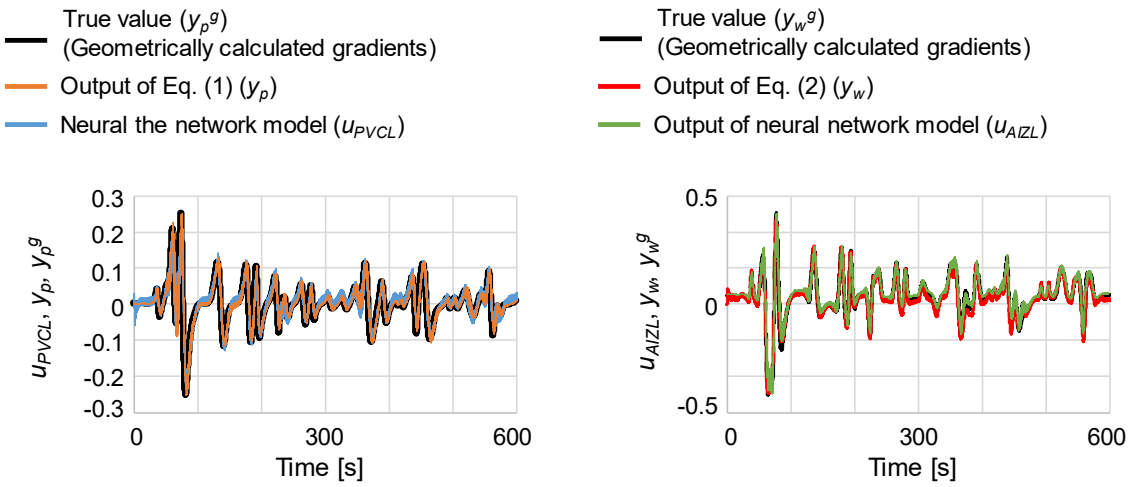

(a) Gradient parallel to the traveling direction

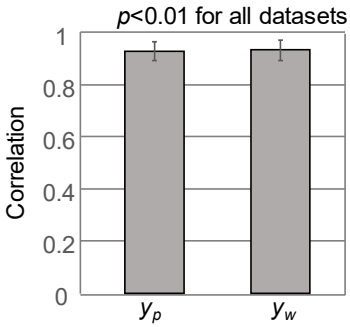

(c) Correlation between the gradients generated by the computational model and the neural network model

Figure 8. Comparison among the true gradients, the outputs of the neural network model, and the outputs of the computational model.

(a) shows the comparison of the gradients parallel to the travelling direction. **(b)** shows the comparison of the gradients perpendicular to the travelling direction. **(c)** shows the average correlation between the neural network model and the computational model. The average correlations were calculated using 10 chemotaxis simulation results partially shown in Fig. 4. The error bars represent the standard deviations.

3.3.3 Ablation Simulation

The trained model was used to simulate laser ablation experiments. The output of ASEL and ASER neurons were respectively fixed to 0, which corresponds to their laser ablation. Figure 10(a) show comparison of the average correlation of simulation and experimental pirouette index values, and Fig. 10(b) show that comparison of the average correlations to weathervane index values. This result shows that the ASER sensory neuron is more important for salt chemotaxis than the ASEL sensory neuron.

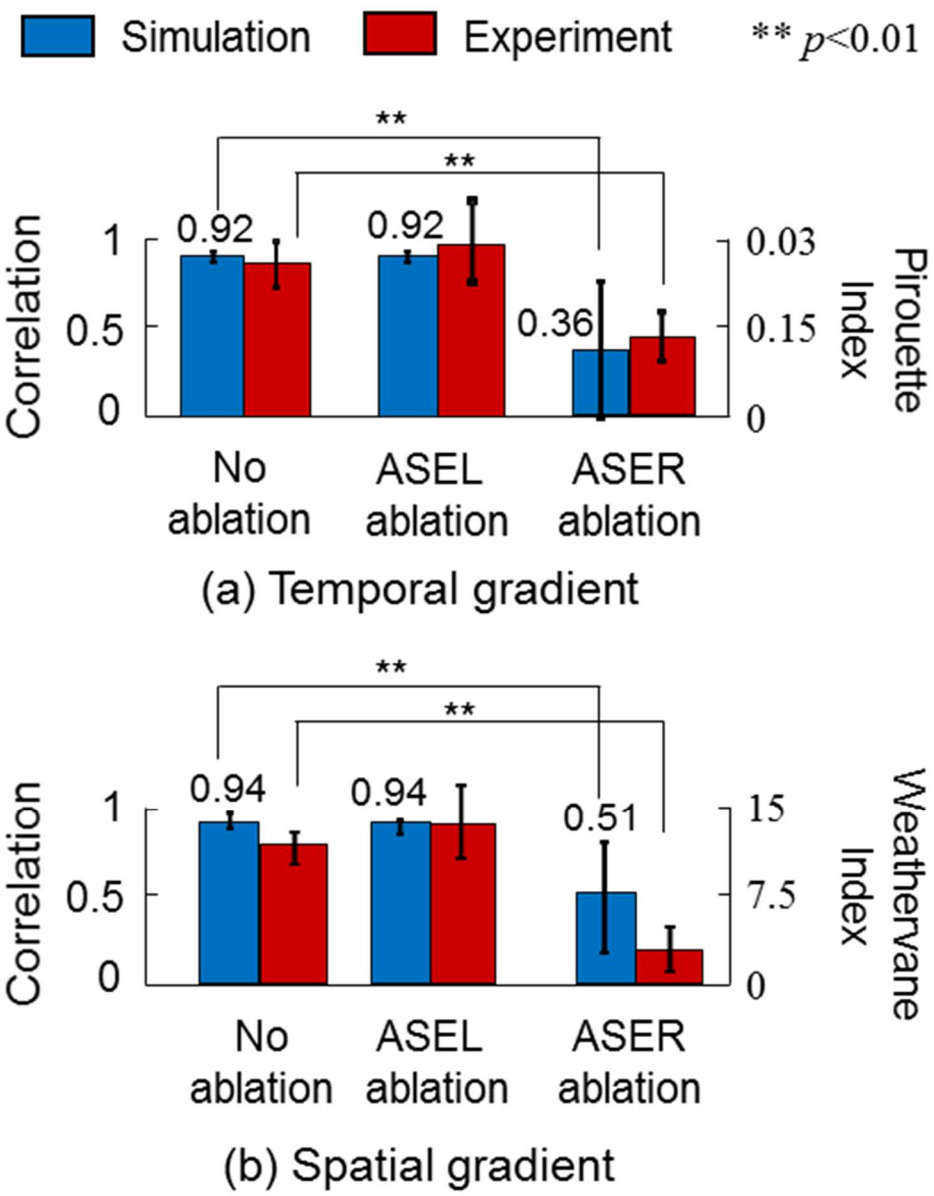

Figure 9. Laser ablation simulation.

The blue bars represent the average correlation between the model outputs and true values of the NaCl gradient and the error bars indicate the standard deviations. The red bars represent experimental results derived from the literature [3]. (a) Comparison of the average correlation of simulation and experimental pirouette index values and (b) comparison of the average correlations to weathervane index values. Bonferroni correction was applied for multiple comparisons.

3.4 Discussion

i. Relationship between NaCl concentration at the nose tip and the internal representations of chemical gradients

This dissertation presents the computational model that can describe the relationships between the chemical concentration sensed at the nose tip of *C. elegans* and the internal representations of chemical gradients closely related to pirouette and weathervane strategies, and tests if the computational model is implementable in the connectome-based neural network model. This analysis concept is based on Marr's level of analysis where the computational model corresponds to the analysis on the computational level, and the neural network simulation corresponds to the analysis on the implementational level.

To verify the computational model, we constructed a chemotaxis simulator which includes the environment model expressing NaCl distribution and the multibody model of *C. elegans*. The results shown in Fig. 4 and the supplemental data indicate that the chemotaxis simulator has the ability to simulate the behaviour during chemotaxis, and is therefore applicable for testing equations (13) and (14). Figure 5 then confirms that equations (13) and (14) could convert the NaCl concentration sensed at the nose tip into the internal representation of the NaCl gradient parallel and perpendicular to the travelling direction. Equation (14) indicates that generating the internal representation of the gradient perpendicular to the travelling direction requires the head-bending angle. It is commonly considered

that head bending is generated by a central pattern generator[16] involving stretch receptors[37]; thus, its information may be obtained through these neurons.

The derivation process (see S2 Appendix 2) shows that the directional decomposition of the time derivative of NaCl concentration requires cosine (symmetric) and sine (asymmetric) functions of the head-bending angle, respectively, for parallel and perpendicular to the travelling direction. Similar decomposition process could be performed in the pair of AIY neurons or their upstream neurons because the results of an experimental study[4] indicated that the symmetric input of the pair of AIY neurons controls the pirouette frequency and the asymmetric input controls the gradual turn (weathervane).

In addition, one of the findings of the model study by Izquierdo & Beer[9] indicated that the asymmetrical response characteristics of the ventral and dorsal motor neurons are required to perform gradual turns (weathervane). That is, the response characteristic of either side of the motor neuron would be shifted to the region of lower sensitivity and the other side to that of higher sensitivity, by the sensory input, so that the motor neurons generate a biased sinusoidal wave to regulate body motion. From the computational model (equation (14)), it can be interpreted that the motor neurons perform the directional decomposition, and the gradient parallel to the travelling direction is coded in the motion of the animal.

As described above, the proposed computational model suggests that both findings obtained from

the observation of AIY neurons and motor neurons in the simulation could be explained by directional decomposition. From the viewpoint of Marr's level of analysis, the computational model can bridge the gap between the problem defined in the computational level and implementational level.

ii. Generating internal representations of chemical gradients based on the neural network structure of *C. elegans.*

Figure 8 confirms that the training algorithm successfully adjusted the parameters of the neural network model and that it could internally represent gradients with respect to the travelling direction using the NaCl concentration sensed at the nose tip and the head-bending angle. High correlations between the respective gradients generated by the computational model, neural network model, and geometrical calculation (shown in Fig. 9) indicate that the computational model can be implemented in the connectome-based neural network.

3.5 Conclusion Remarks

In this study, a simple and comprehensive computational model was derived to convert the response of a single sensory input into two types of internal representations of the NaCl gradient parallel and perpendicular to the travelling direction and enabled simultaneous simulation of the pirouette and weathervane strategies. The derived computational model suggests that internal representations of the gradients can be generated by combining head-bending angles and sensory input from ASEL/R

neurons. It could also be used to interpret the functions of AIY neurons and motor neurons, respectively, identified in previous experimental[4] and simulation studies[9] and thus can bridge the gap between the chemotaxis problems at the computational and implementational levels.

The connectome-based neural network model included in the chemotaxis simulator demonstrated that the computational model could be implemented in it, although the coding manner of the chemical gradient might differ from that of the actual animals. The connectome-based neural network model may allow further analysis of the functions of respective neurons by introducing the biological constrictions and measured neural activities and by simulating ablation experiments.

Chapter 4

4 Muscle Activity Generation Model and Simulation

4.1 Introduction

This chapter is organized as follows: Section 4.2 describes the how to make teacher signal using *C. elegans* expressing fluorescent proteins on its body wall muscle and connectome-based motor neuron and muscle model. Section 4.3 is the result of the simulation and we discuss the result in Section 3.4. Finally, Section 3.5 concludes the chapter.

4.2 Materials and Methods

4.2.1 Fluorescent Amount Associated with Muscle Activity

To clarify the relationship between muscle activities and local body-bending angles, we recorded a video of an animal freely moving on an agar plate by using a stereomicroscope. In this section, we describe the experimental and analysis methods.

i. Strain

In this study, we employed a transgenic strain (HBR4: *goeIs3[pmyo-3::GCamP3.35::unc-54-3' utr; unc-119(+)]V*) [38] of *C. elegans* expressing fluorescent proteins on its body wall muscle. The animals were cultured in an incubator at 20 degrees Celsius [39] over three days after hatching on the

Nematode Growth Media (NGM) agar plate on which Escherichia coli (E. coli) OP50 was spread. The *C. elegans* strain and E. coli were obtained from the Caenorhabditis Genetics Center (University of Minnesota).

ii. Video Recording

We transferred an animal to the NGM agar plate one by one. Video recording was performed in a dark room using an epifluorescence microscope (SZX16, Olympus, Tokyo, Japan) on which an LCD digital camera (EX-F1, Casio computer, Tokyo) was mounted. The settings of the stereomicroscope and recording conditions are as follows.

> Settings of stereomicroscope

Objective lens ratio: 6.4

Excitation light source: Xenon lamp

Filter: Band-pass filter at wavelengths of 490–560 nm

> Recording conditions

Resolution: 480 × 640 [pixel]

Frame rate: 29.97 [fps]

iii. Extracting Local Bending Angles

This section explains the procedures used to extract the local body-bending angles and fluorescence intensity at the corresponding location from the recorded video images.

First, we binarized the video images and tracked the body using an image processing software (MoveTr2D; Library, Tokyo, Japan) and worm-tracking software (Wriggle Tracker; Library, Tokyo, Japan), respectively. To binarize the video image, the weighted sum of RGB components, $R(x,y)$, $G(x,y)$, and $B(x,y)$, at pixel coordinates (x,y) was calculated using the following equation for each frame.

$$F(x,y) = w_r R(x,y) + w_g G(x,y) + w_b B(x,y), \tag{27}$$

$$Y(x,y) = \begin{cases} 1 & (F(x,y) < F_{th}) \\ 0 & (F(x,y) \geq F_{th}) \end{cases}, \tag{28}$$

where F_{th} is the threshold parameter, and $w_r, w_g, and\ w_b$ represent the weights of the RGB components. These parameters were determined by trial and error. The noise in the video image was removed by dilation and erosion processing, followed by the application of a median filter. The pixel with $Y(x,y) = 0$ was considered as a part of the body, as shown in Fig. 11.

Binarized image $Y'(x,y)$ of the body was thinned and divided into n equal points. The local body-bending angle, $\theta_i(t)$, was then calculated from the coordinates of three adjacent dividing points, $\boldsymbol{p}_{i-1}, \boldsymbol{p}_i, and\ \boldsymbol{p}_{i+1}$ $(\boldsymbol{p}_i = (x_i, y_i),\ i = 2,3,\dots,n-1))$, at each sampling time t. Angular velocity $\dot{\theta}_i(t)$ and angular acceleration $\ddot{\theta}_i(t)$ were calculated by applying a time differential filter once and

twice, respectively.

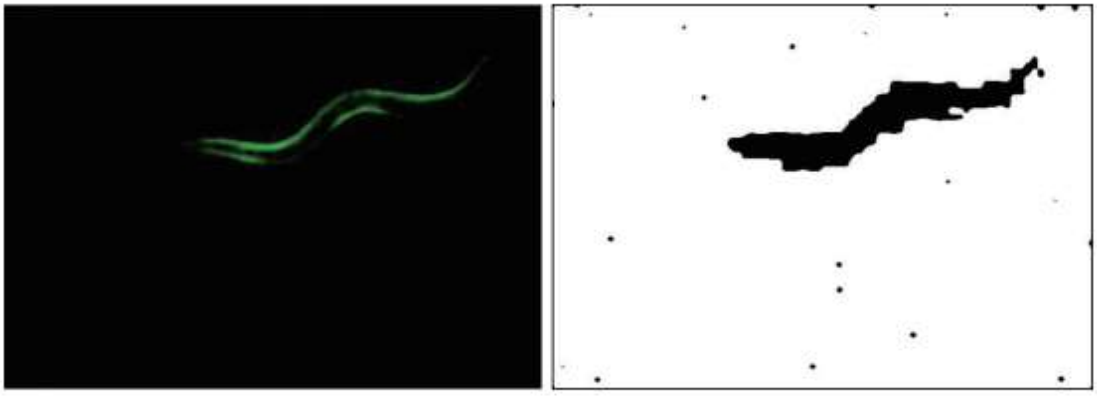

Figure 10. Fluorescence image and binarized image

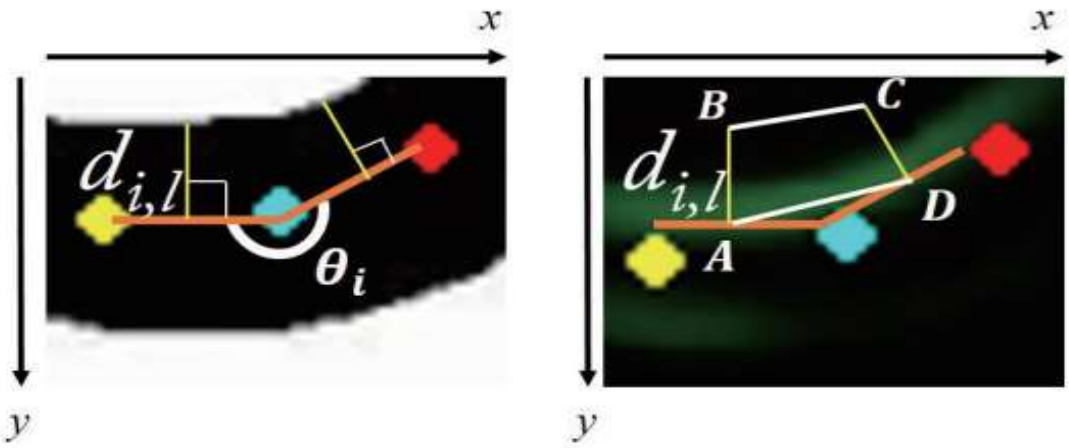

Figure 11. Measurement of distance $d_{i,l}$ and configuration of the quadrangle for fluorescence strength extraction in the experimental and analysis methods

iv. Extracting Fluorescence Intensity

Based on the midpoint of the straight line connecting two adjacent dividing points, vertical unit vector $v_i = (a_i, b_i)$ was calculated with respect to the straight line, as shown in Fig. 12, and distance $d_{i,l}(l \in \mathrm{D}, \mathrm{V})$ from the midpoint to the outside of the body was measured, where D represents dorsal, and V represents ventral. We defined a unit sign scalar, $\delta \in \{+1, -1\}$, and scanned coordinates $\boldsymbol{h}_k = (\boldsymbol{p}_{i-1} + \boldsymbol{p}_i)/2 + k\delta\boldsymbol{v}_i$ by incrementing k $(k = 1,2, \ldots, K)$. The distance was then defined as $d_{i,l} = k\delta$ when $Y'(\boldsymbol{h}_{k-1}) = 1$ changed to $Y'(\boldsymbol{h}_k) = 0$. If $Y'(\boldsymbol{h}_k)$ did not change to 0 after scanning up to K or if $Y'(\boldsymbol{h}_0) = 1$ at $k = 0$, the video image was considered unanalyzable and the frame was skipped. Because the animal moved on the agar surface by alternately contracting and relaxing the ventral and dorsal muscles, we measured $d_{i,l}$ in both the positive and negative directions of δ and assigned the distance to either the dorsal or ventral sides. Based on $\boldsymbol{p}_i$ and corresponding distance $d_{i,l}$, a quadrilateral with vertices' coordinates $\boldsymbol{A}_{i,l}, \boldsymbol{B}_{i,l}, \boldsymbol{C}_{i,l}, \boldsymbol{and}\ \boldsymbol{D}_{i,l}$ was created on the video image, as shown in Fig. 12, where $\left(\boldsymbol{A}_{i,l} = \boldsymbol{p}_i + \boldsymbol{p}_{i-1}/2, \boldsymbol{B}_{i,l} = \boldsymbol{A}_{i,l} + \delta d_{i,l}\boldsymbol{v}_i, \boldsymbol{C}_{i,l} = \boldsymbol{D}_{i,l} + \delta d_{i,l}\boldsymbol{v}_{i+1}, \text{and} \boldsymbol{D}_{i,\mathrm{l}} = (\boldsymbol{p}_i + \boldsymbol{p}_{i+1})/2\right)$.

The fluorescence intensities of the pixels inside quadrilateral $\boldsymbol{A}_{i,l}\boldsymbol{B}_{i,l}\boldsymbol{C}_{i,l}\boldsymbol{D}_{i,l}$ were averaged to represent the local muscle activity induced by the calcium current. Here, a pixel at coordinate $\boldsymbol{P} = (x,y)$ was considered to be inside the quadrilateral if it satisfied the following equations:

$$\sigma_1 = \sigma_2 = \sigma_3 = \sigma_4$$

$$\begin{aligned}
\sigma_1 &= sgn\{(\boldsymbol{B_{i,l}} - \boldsymbol{A_{i,l}}) \times (\boldsymbol{P} - \boldsymbol{A_{i,l}})\} \\
\sigma_2 &= sgn\{(\boldsymbol{C_{i,l}} - \boldsymbol{B_{i,l}}) \times (\boldsymbol{P} - \boldsymbol{B_{i,l}})\} \\
\sigma_3 &= sgn\{(\boldsymbol{D_{i,l}} - \boldsymbol{C_{i,l}}) \times (\boldsymbol{P} - \boldsymbol{C_{i,l}})\} \\
\sigma_4 &= sgn\{(\boldsymbol{A_{i,l}} - \boldsymbol{D_{i,l}}) \times (\boldsymbol{P} - \boldsymbol{D_{i,l}})\}.
\end{aligned} \tag{3}$$

The fluorescence intensity, $L(\boldsymbol{P})$, at coordinate $\boldsymbol{P}$ was under threshold L_{th} was considered as noise and was not included in the calculation for average fluorescence intensity. The averaged florescence intensity was normalized so that the maximum value was 1 and the minimum value was 0 for each quadrilateral. The normalized average fluorescence intensity was denoted as $M_{i,l}(t)(l \in D, V)$ on the l side of dividing point i.

v. Correlation and Multiple Regression Analysis

To analyze the relationship between the local body-bending angles and the muscle activity, the partial correlation coefficients of $M_{i,l}(t)$ against $\theta_i(t)$, $\dot{\theta}_i(t)$, and $\ddot{\theta}_i(t)$ were calculated. Multiple regression analysis was also performed on all division points of the analysis image using the following equation:

$$\boldsymbol{M_l} = \mathrm{a}_{1,l}\,\boldsymbol{\theta_l} + \mathrm{a}_{2,l}\dot{\boldsymbol{\theta}}_{\boldsymbol{l}} + \mathrm{a}_{3,l}\ddot{\boldsymbol{\theta}}_{\boldsymbol{l}} + \mathrm{b}_l, \tag{30}$$

where ventral and dorsal muscle activities $\boldsymbol{M_l} = [\boldsymbol{M}_l(0)^T, \dots, \boldsymbol{M}_l(T)^T]^T$ ($\boldsymbol{M}_l(t) = [M_{1,l}(t), \dots, M_{n-1,l}(t)]$) are objective variables, and angle $\boldsymbol{\theta} = [\boldsymbol{\theta}_1(0)^T, \dots, \boldsymbol{\theta}_{n-1}(T)^T]^T$ ($\boldsymbol{\theta}(t) = [\theta_1(t), \dots, \theta_{n-1}(t)]$), angular velocity $\dot{\boldsymbol{\theta}}_i = \left[\dot{\boldsymbol{\theta}}_1(0)^T, \dots, \dot{\boldsymbol{\theta}}_{n-1}(T)^T\right]^T$ ($\dot{\boldsymbol{\theta}}(t) = [\dot{\theta}_1(t), \dots, \dot{\theta}_{n-1}(t)]$), and angular acceleration $\ddot{\boldsymbol{\theta}}_i = \left[\ddot{\boldsymbol{\theta}}_1(0)^T, \dots, \ddot{\boldsymbol{\theta}}_{n-1}(T)^T\right]^T$ ($\ddot{\boldsymbol{\theta}}(t) = [\ddot{\theta}_1(t), \dots, \ddot{\theta}_{n-1}(t)]$) are explanatory variables.

vi. Experimental Configurations

We recorded video images of three individuals and analyzed each individual for 5 s. The weights of the RGB components were set to w_r= 0.2989, w_g= 0.5870, and w_b= 0.1140. The maximum number of scans was set to K = 200. The fluorescence intensity threshold was $L_{th} = 45$.

4.2.2 Connectome-based Motor Neuron and Muscle Model

Figure 1 shows the connection diagram of the model based on the connectome described in the nematode database WormAtlas [34]. In particular, the model consists of five pairs of ten command interneurons, seven types of 69 motor neurons, and four rows of 95 muscles [1,17,34]. The neurons and muscles are connected based on the adjacency matrix of the synaptic and gap connections accessible from the following URL: https://wormwiring.org/pages/adjacency.html [34].

The command interneurons are comprised of PVCL/R and AVBL/R (responsible for forward movement), in addition to AVAL/R, AVDL/R, and AVEL/R (responsible for backward movement) [12]. We assumed that the command interneurons have no specific polarity, and do not include an oscillating component to generate periodic muscle contractions [18-20,40].

Motor neurons control the muscles based on the outputs of the command neurons and are comprised of DB, DA, DD, VB, VD, VA, and AS (indicated by circles in Fig 13). Acetylcholinergic neurons, DB, DA, VB, VA, and AS were assumed to excite VD, DD, and muscles. GABAergic neurons VD and DD then inhibit the acetylcholinergic neurons and muscles. Although the polarities of the synaptic connections were determined based on the description in a previous study [1,34], they have not been fully confirmed experimentally. Therefore, it should be noted that these connections have the potential to be either excitatory or inhibitory in an actual animal.

Proprioceptive feedback also plays an important role in generating undulatory movements, and the undifferentiated processes extending from A- and B-class motor neurons are responsible for proprioceptive feedback [18]. Because the model does not contain the body in order to focus on the neuromuscular system, we connected several muscles to an anterior A-class neuron and a posterior B-class neuron to represent proprioceptive feedback, assuming that muscle activity correlates with body curvature. Here, we did not impose the polarities of the proprioceptive feedback connections.

In Fig 13, the *C. elegans* muscle indicated by the ellipse is composed of 95 cells arranged in four

rows, and the ventral and dorsal muscle cells alternately contract and relax to produce a smooth crawling motion. For simplification, we assumed the simultaneous activation in each left and right muscle pair, considering their two-dimensional movement on the agar. We trained the model using backpropagation through time, a supervised algorithm, to generate muscle activity patterns using two types of teacher data: a mathematically defined sinusoidal pattern, and an activity pattern measured from a fluorescence strain (HBR4).

The command interneurons consist of forward command neurons (PVCL/R, AVBL/R) and backward command neurons (AVAL/R, AVBL/R, AVEL/R) that output control signals of 1 or 0. An output of 1 represents the activated state, and 0 represents the resting state. As shown in the following equations, the forward command neuron $L_a(t)$ outputs 1 and the backward command neuron $L_c(t)$ outputs 0 during a preset time $[T_{2v-1}, T_{2v})$ $(v = 1, 2, \dots, o)$ to command forward movement. This output is reversed during $[T_{2v}, T_{2v+1})$ to command backward movement:

$$L_a(t) = \begin{cases} 1 & (T_{2v-1} \le t < T_{2v}) \\ 0 & (T_{2v} \le t < T_{2v+1}) \end{cases}, \tag{31}$$

$$L_c(t) = \begin{cases} 0 & (T_{2v-1} \le t < T_{2v}) \\ 1 & (T_{2v} \le t < T_{2v+1}) \end{cases}, \tag{32}$$

where $L_a(t)$ is the output of the forward command neurons (PVCL/R, AVBL/R) and $L_c(t)$ is the output of the backward command neurons (AVAL/R, AVBL/R, AVEL/R). The index a = 1, 2, 3, 4 corresponds to a total of four forward command neurons, and c = 5, 6, ..., 10 corresponds to a total of six backward command neurons.

In the motor neurons, a muscle contraction pattern is generated based on the output of the command neuron. The motor neuron is defined by the following equations:

$$x_i^N(t+1) = \frac{1}{1+F_s\tau_i}x_i^N(t) + \frac{F_s\tau_i}{1+F_s\tau_i}\left\{\sum_{j=1}^{J} w_{ij}^{NN} y_j^N(t) + \sum_{u=1}^{U} w_{iu}^{MN} y_u^M(t)\right.$$

$$+\sum_{j=1}^{J} g_{ij}^{NN}\left(x_j^N(t) - x_i^N(t)\right) + \sum_{u=1}^{U} g_{iu}^{MN}\left(x_u^M(t) - x_i^N(t)\right) \quad (33)$$

$$\left.+\sum_{p=1}^{P} w_{ip}^{IN} L_p(t) + I_{\mathrm{p}i}(t) + w_i^{l0}\right\}$$

$$y_i^N(t) = \frac{1}{1+\exp\left(-x_i^N(t)\right)} \quad (34)$$

where $x_i^N(t)$ and $x_u^M(t)$ are currents flowing into motor neuron *i* and muscle *u* at time *t,* respectively; $y_i^N(t)$ and $y_u^M(t)$ are membrane potentials of motor neurons and muscles, respectively; ω_i^{l0} is the bias, τ_i is the first-order lag element, and F_s is the sampling frequency configured in the simulation procedure. ω_{ij}^{NN}, ω_{iu}^{MN}, ω_{ip}^{IN} are weights representing the synaptic connection strength among motor neurons, that from muscle to motor neuron, and that from the command neuron to motor neuron, respectively. $g_{ij}^{NN} = g_{ji}^{NN}$, $g_{iu}^{MN} = g_{ui}^{MN}$ are weights corresponding to the conductance of the gap junctions. $J = 69$ is the number of motor neurons, $P = 10$ is the number of command neurons, and $U = 95$ is the number of muscle cells. $I_{\mathrm{p},i}(t)$ represents the proprioceptive feedback to the A- and B-class motor neurons determined by the following equation.

$$I_{\mathrm{pi}}(t)=\begin{cases}\sum_{u=1}^{S} w_{i\{3(i+1)-u\}}^{MN} y_{\{3(i+1)-u\}}^{M}(t), & i \in \text{B– class motor neuron} \\ \sum_{u=1}^{S} w_{i\{3(i+1)+u\}}^{MN} y_{\{3(i+1)+u\}}^{M}(t), & i \in \text{A– class motor neuron} \\ 0, \quad \text{Otherwise} & \end{cases} \tag{4}$$

Here, $w_{i\{3(i+1)-u\}}^{MN}$ denotes the connection strength, $3(i+1)-u$ and $3(i+1)+u$ are the indexes of a muscle, and we set the proprioceptive feedback length as $S=7$ muscles. For the motor neurons located at the head and tail, *S* was set to the number of the existing anterior and posterior muscles. In this configuration, an A- and B-class neuron receives the outputs from up to seven anterior and posterior muscles.

When the muscles receive the output from the motor neurons, they output the muscle activation level according to the following equations:

$$\begin{aligned} x_u^M(t+1) = & \frac{1}{1+F_s\tau_u} x_u^M(t) \\ & + \frac{F_s\tau_u}{1+F_s\tau_u}\left\{\sum_{j=1}^{J} \omega_{uj}^{NM} y_j^N(t) + \sum_{j=1}^{J} g_{uj}^{MN}\left(x_j^N(t)-x_u^M(t)\right)\right. \\ & \left. + \sum_{k=1}^{K} g_{uk}^{MM}\left(x_k^M(t)-x_u^M(t)\right) + \omega_u^{l1}\right\} \end{aligned} \tag{5}$$

$$y_u^M(t) = \frac{1}{1+\exp\left(-x_u^M(t)\right)}, \tag{6}$$

where ω_{uj}^{NM} is a weight representing the synaptic connection strength from the motor neuron to muscle, and g_{uk}^{MM} is a weight representing the conductance of the gap junctions between the muscle, $K = 95$ is the number of muscle cells.

According to the connectome data [34], the absence of connections was represented by restricting

the weights of the synapse connection and gap junction to 0 during the following training. The following constraint condition is set for each parameter based on the type of connections.

The parameters of the neural network model (first-order lag element, synaptic connections, and gap junctions) are trained using the BPTT algorithm [21]. The evaluation function is defined as:

$$E = \frac{1}{T}\frac{1}{U}\sum_{t=1}^{T}\sum_{u}^{U}\frac{1}{2}\{y_u^M(t) - d_u(t)\}^2, \tag{38}$$

where $d_u(t)$ is the teacher data, $y_u^M(t)$ is the activity level of the muscles, and T is the maximum step number of the simulation time. BPTT updates each parameter in a particular direction to minimize the evaluation function, which is determined by partial differentiation of the evaluation function for the corresponding parameter. In addition, the following constraint condition is set for each parameter based on the type of connections.

・The synaptic connection strengths from the excitatory neurons DA ($i = 1, 2, \ldots, 8$), DB ($i = 9, 10, \ldots, 16$), VA ($i = 23, 24, \ldots, 34$), VB ($i = 35, 36, \ldots, 45$), and AS ($i = 59, 60, \ldots, 69$) are constrained to positive values.

・The synaptic connection strengths from inhibitory neurons DD ($i = 17, 18, \ldots, 22$) and VD ($i = 46, 47, \ldots, 58$) are constrained to negative values.

・The first-order lag elements τ_i, τ_u are constrained to positive values ($\tau_i \geq 0$).

The teacher data $d_u(t)$ used for parameter adjustment are generated based on the motion analysis of *C. elegans*. As shown in Fig 14, we tracked seven points on the body of *C. elegans* while

performing forward movement and plotted the time change of the angles between the two straight lines connecting adjacent points. In the figure, each angle shows a sinusoidal-like waveform that is transmitted from the head to the tail. Because the movement of *C. elegans* is generated by alternating activities of the muscles, the activity level is considered to have similar characteristics. Therefore, we express the teacher data for the activity level of the muscles according to equations (39)–(41).

In the first period of forward movement $(T_1 \leq t < T_2)$, when the index q = 1, 2, …, 24 is sequentially defined for the muscles from the head to the tail, the teacher data for the left dorsal (u = 1, 2, …, 24) and the right dorsal (u = 25, 26, …, 48) muscles are given by the following equation:

$$d_u(t) = \sin\left(\omega t + \phi_u(t)\right) \quad (u = 1, 2, \dots, 24, 25, 26, \dots, 48), \tag{7}$$

where phase $\phi_u(t), \left(\phi_u(0) = -\frac{\pi q}{12}\right)$ is changed when switching between forward and backward movement at a time $T_v(v > 1)$ as defined below.

$$\phi_u(t) = \pi - 2\omega T_v - \phi_u(T_{v-1}), \tag{40}$$

Similarly, the left and right ventral muscle $(u = 49, 50, \dots, 72, 73, 74, \dots, 95)$ are assumed to be active in opposite phases to the dorsal muscle cells, and are given by the following equation:

$$d_u(t) = \sin\left(\omega t - \pi + \phi_u(t)\right) \quad (u = 49, 50, \dots, 72, 73, 74, \dots, 95). \tag{41}$$

Based on measured data, the angular frequency is set to $\omega = 1.6\pi$.

In addition, we measured the muscle activities using a strain expressing calcium indicator in the body-wall muscle (HBR4: *goeIs3[pmyo-3::GCamP3.35::unc-54-3' utr, unc-119(+)]V*) [38], and

trained the model using the measured fluorescence rate. We followed procedures in the literature [41] to measure the fluorescence intensity of the body-wall muscles. As shown in Fig 15, a video analysis software (WormLab, MBF Bioscience, Williston, USA) was used to track the body outline of the animal, and then the body was divided into 24 equal segments from the head to the tail. The fluorescence intensities at the dorsal (k = d) and ventral (k = v) sides of the divided i-th segment $F_{i,t}^{k}$ were measured in the ventral and dorsal areas of each segment, and converted to fluorescence rates $((F_{i,t}^{k} - F_{0,i}^{k})/F_{0,i}^{k})$, where $F_{0,i}^{k}$ is the minimum fluorescence intensity at the k side of the i-th segment. The fluorescence rates were fitted to multiple sinusoidal functions, as expressed by the following equation, to smooth the measured data:

$$d_u(t) = \sum_{i=1}^{n} a_{ui} \sin(\omega_{ui} t + \phi_{ui}), \tag{8}$$

where $n = 8$ is the number of the functions, t is the time, a_{ui}, ω_{ui}, and ϕ_{ui} are the amplitude, frequency, and phase of the i-th sinusoidal function, respectively. The fitted data were then concatenated to generate three cycles of forward and backward movement. The value of fluorescence intensity was normalized to a range [0.25, 0.75], and used as the teacher data to train the model.

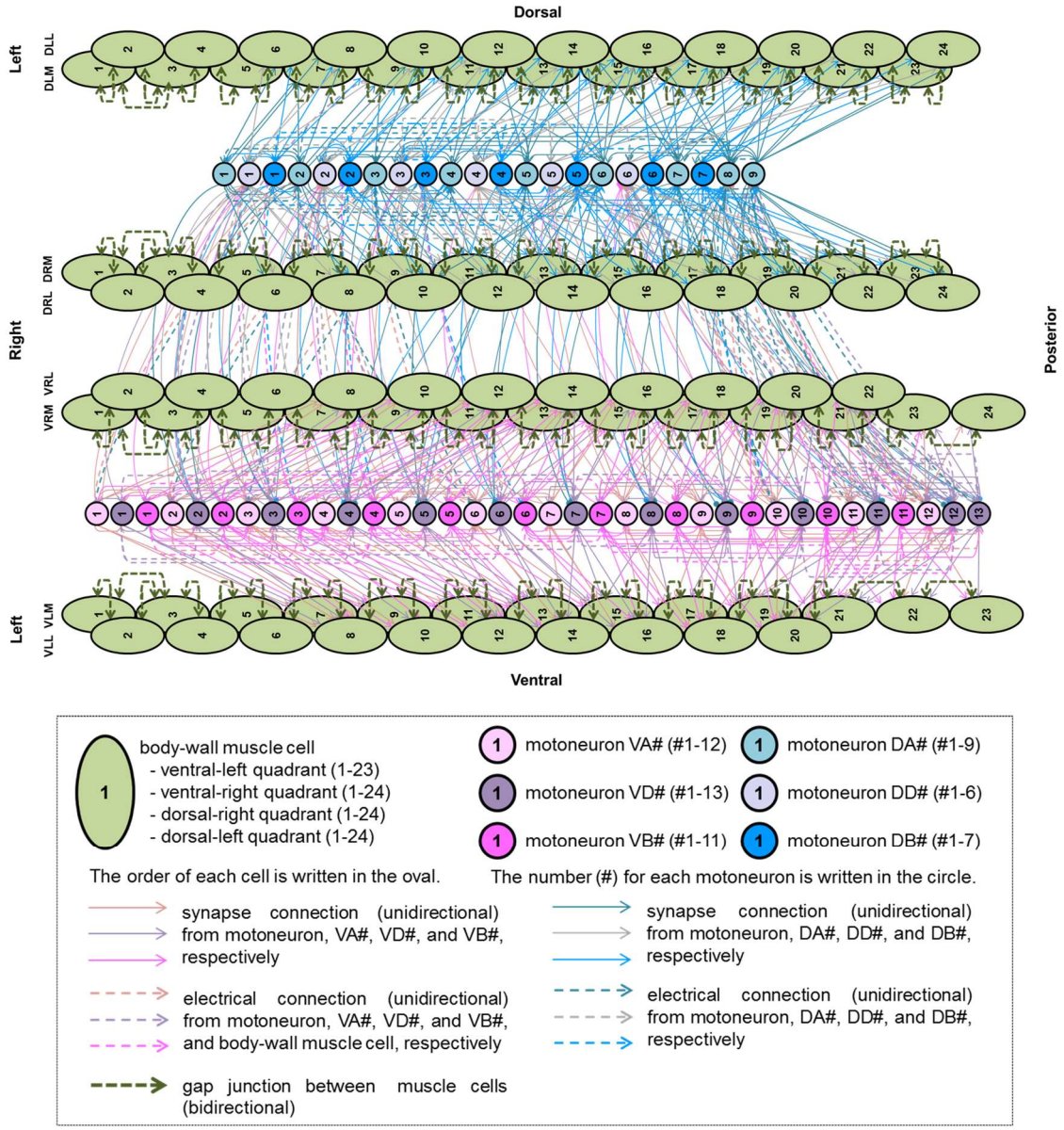

Figure 12. Diagram of neuro-muscular connections illustrated based on the WormAtlas database [5].

Synaptic connections and gap junctions of whole muscle cells (total 95) and motor neurons VA, VD, VB, DA, DD, and DB. The green oval represents the body-wall muscles, the upper side of the figure is the anterior direction, the lower side is the posterior direction, and, starting from the left row, it shows the left ventral side, right ventral side, left dorsal side, and right dorsal side. The circles represent motor neurons, and the difference in color corresponds to the types of motor neurons, as shown in the legend. Solid lines represent synaptic connections, and dotted lines represent gap junctions.

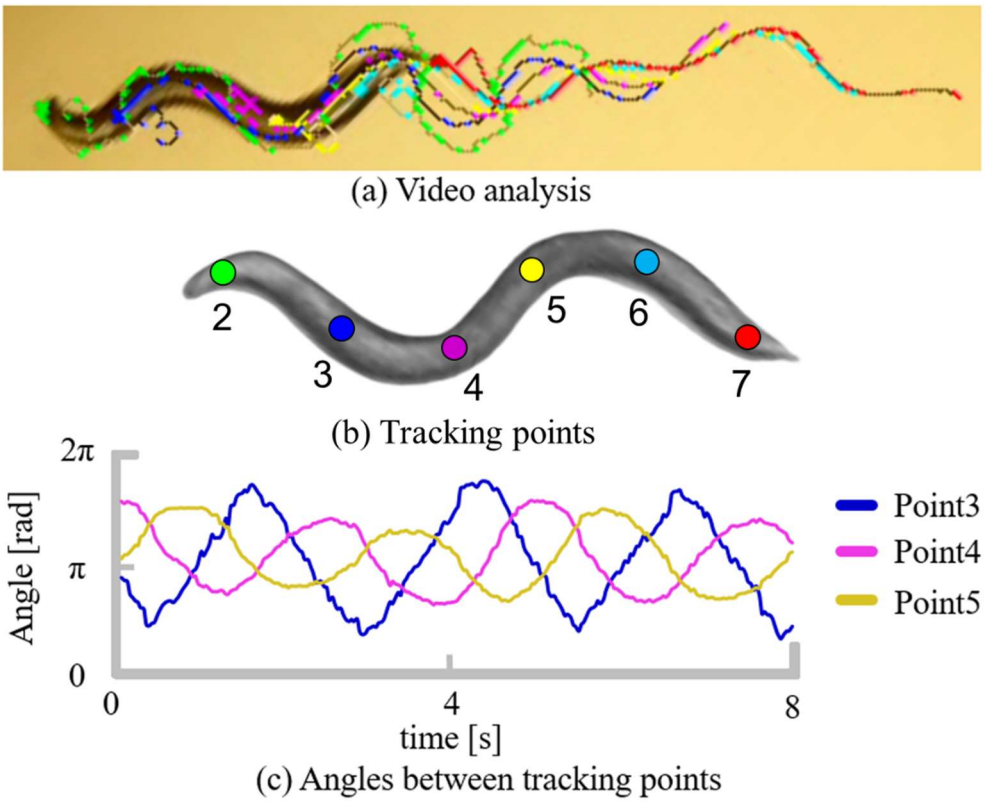

Figure 13. Motion analysis of *C. elegans*.

(A) Motion analysis capture of *C. elegans* using the image analysis software Wriggle tracker (Library Inc., Tokyo). (B) Points tracked by the image analysis software. (C) Temporal change in the angles between the straight lines connecting adjacent points.

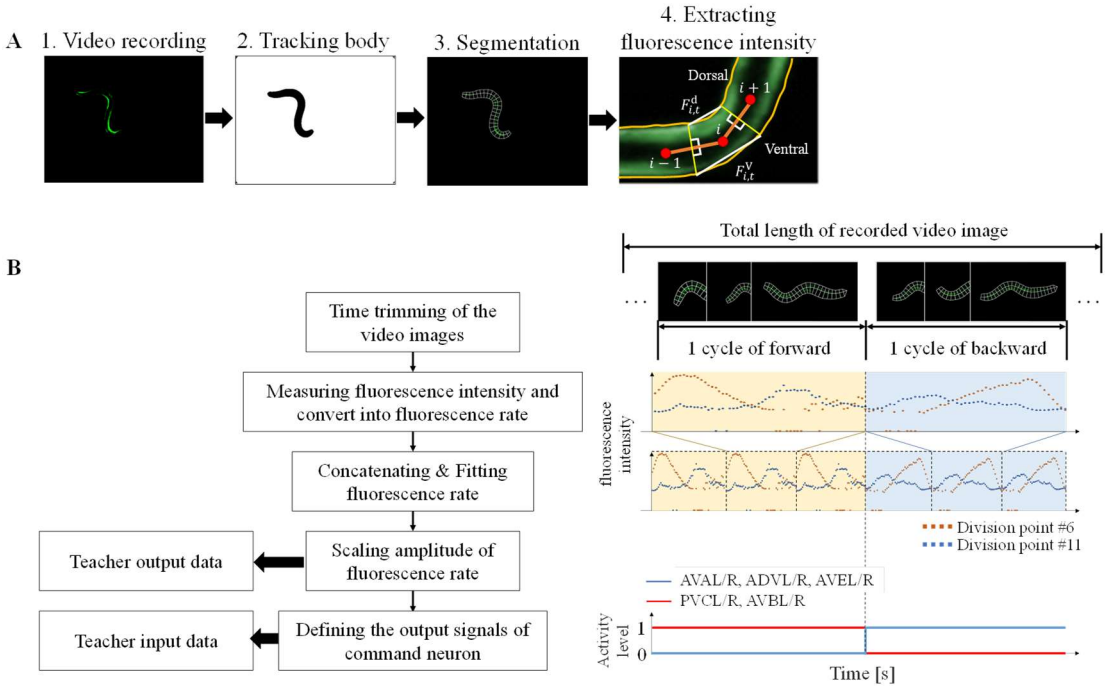

Figure 14. Measurement of fluorescence intensity.

(A) The measurement procedure. The body is divided into i = 1, 2 …, 24 segments using a video analysis software (WormLab, MBF Bioscience, Williston, USA). The average fluorescence intensities were extracted at the dorsal and ventral sides of the i-th segment. (B) Procedure of teacher data preparation. The left shows the block diagram of data preparation, and the right shows the corresponding images.

4.2.3 Simulation Configurations

The teacher data for training was configured as follows: the simulation time was set to T = 30 s, and the sampling frequency was set to F_s = 0.05 s, the time for switching between forward and backward movement was set to T_1 = 0.0, T_2 = 8.7, T_3 = 17.6, T_4 = 22.8, T_5 = 26.6. The initial value of each parameter was set at random according to a uniform distribution within the following range.

・The excitatory synaptic connection $\omega_{ij}^{NN}, (i = 1\text{–}8,\ 9\text{–}16,\ 23\text{–}34,\ 35\text{–}45, -69)$: [0, 1]

$$\omega_{ui}^{NM}, (j = 1\text{–}8,\ 9\text{–}16,\ 23\text{–}34,\ 35\text{–}45): [0, 1]$$

・The inhibitory synaptic connection $\omega_{ij}^{NN},\ (i = 17\text{–}22,\ 46\text{–}58)$: [−1, 0]

$$\omega_{ui}^{NM}, (i = 17\text{–}22,\ 46\text{–}58): [-1, 0]$$

・The synaptic connections $\omega_{iu}^{MN},\ \omega_{ip}^{IN},\ \omega_{i}^{l0},\ \omega_{u}^{l1}$: [−1, 1]

・The gap junctions $g_{ij}^{NN},\ g_{iu}^{MN},\ g_{uk}^{MM}$: [0, 1]

・The first-order lag elements $\tau_i,\ \tau_u$: [0, 0.01]

The iterative adjustment of parameters terminates when the evaluation function (Eq. (38)) satisfies $E \leq 0.005$.

Figure 16 A illustrates the teacher data generated using equations (31), (32), and (39), and B shows the teacher data generated using the measured muscle activity. The same teacher data were used to train the ipsilateral side, assuming movement on the 2D agar plane. The left part of Fig 16 shows the binary input from the command neurons. Color maps show the teacher data of the muscles. This

figure shows that during forward movement, waves are transmitted from the head to the tail with some phase delay. Conversely, the waves are transmitted from the tail to the head during the period of backward movement. The phase of each wave is reversed at the time when the forward and backward movement switches.

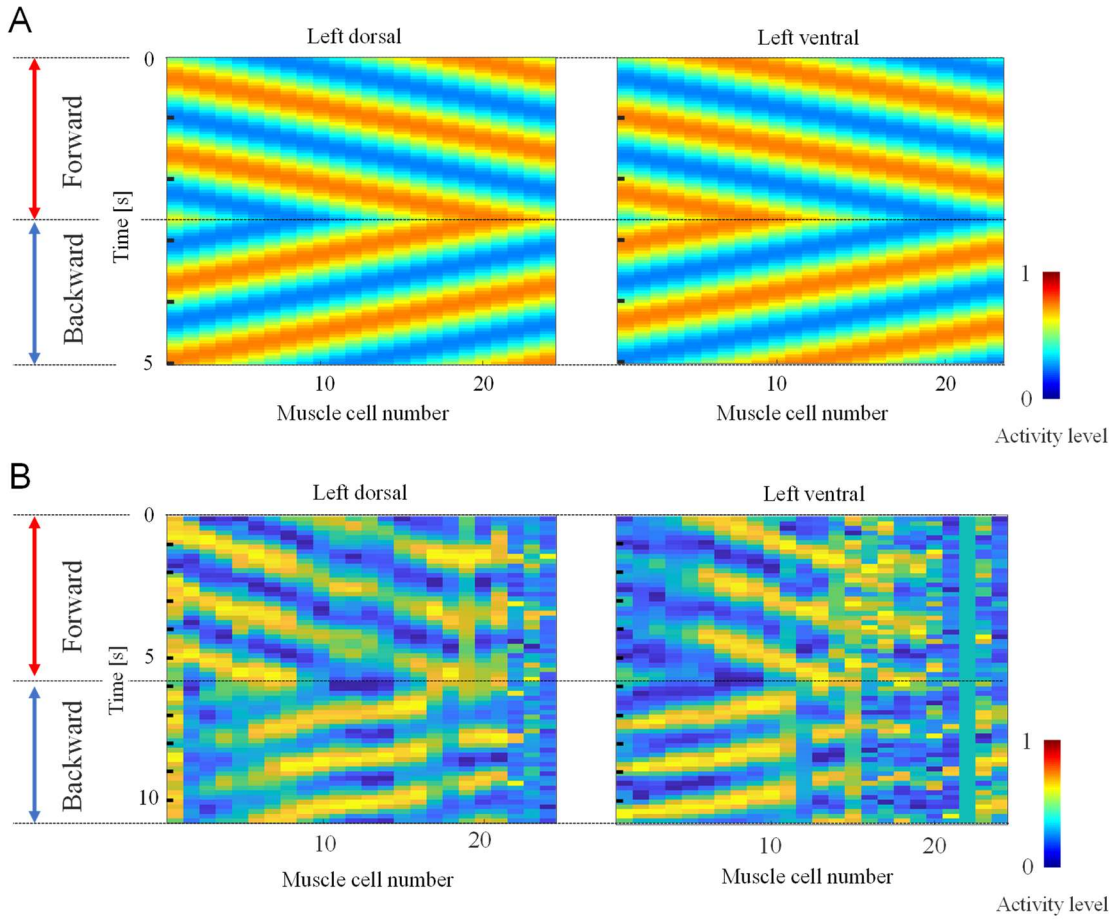

Figure 15. Teacher data for muscles.

(A) Teacher data generated by equations (39)–(41). (B) Teacher data generated using the measured muscle activity. The red arrows represent the time duration of forward movement, and the blue arrows represent the time duration of backward movement. The output switches between forward and backward movement at the predetermined time. The x-axis represents the muscle cell number, indexed from head to tail, the y-axis represents time, and the color represents the teacher data for the muscle activation level. The same teacher data are used for the right side of the body-wall muscles.

4.3 Results

4.3.1 Fluorescent Amount Associated with Muscle Activity

Fig. 15 shows the tracked images. The shape of the body of *C. elegans* was extracted using the method described in sections 2.2 and 2.3, and the fluorescences emitted from body wall muscles were included in the quadrilaterals. Fig. 16 shows the color maps of angle $\theta_i(t)$ and the dorsal and ventral muscle activities, $M_{i,l}$. In the figure, the x-axis represents the dividing point, y-axis represents time, and the color corresponds to the local

body-bending angle and fluorescence rate of each division point, as shown in the color bar. The figure shows that the muscle activity propagates from head to tail when the animal performs a forward movement and propagates from tail to head when the animal performs a backward movement. This figure confirms that contraction and relaxation patterns of muscle were extracted.

To clarify the relationship between movement and muscle, partial correlation coefficients between fluorescence rate $M_{i,l}$ and local body-bending angle θ_i, angular velocity $\dot{\theta}_i(t)$, and angular acceleration $\ddot{\theta}_i(t)$ were calculated. Fig. 19 shows the partial correlation coefficients. In the figure, the x-axis represents angle $\theta_i(t)$, angular velocity $\dot{\theta}_i(t)$, and angular acceleration $\ddot{\theta}_i(t)$, and the y-axis represents the partial correlation coefficient. The figure shows that the partial correlation coefficient between the fluorescence rate and local body-bending angle $\theta_i(t)$ is the highest.

The value of partial regression coefficients $a_1, a_2, and\ a_3$ is shown in Fig. 20. In the figure, the x-axis shows partial regression coefficient $a_1, a_2, and\ a_3$, and the y-axis represents the value of the partial regression coefficients. The coefficient of determination, R^2, was 0.175 for the dorsal side and 0.399 for the ventral side. The analysis results showed that the body bends of *C. elegans,* which are expressed by angle $\theta_i(t)$, angular velocity $\dot{\theta}_i(t)$, and angular acceleration $\ddot{\theta}_i(t)$ could explain the dispersion of fluorescence intensity of 25±12%.

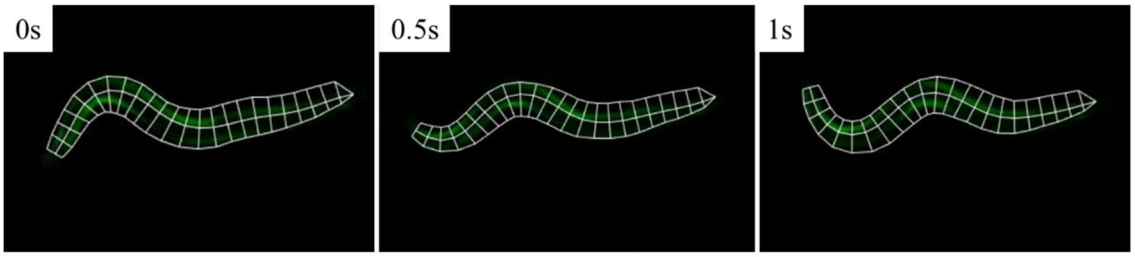

Figure 16. ***C. elegans*** **tracking image**

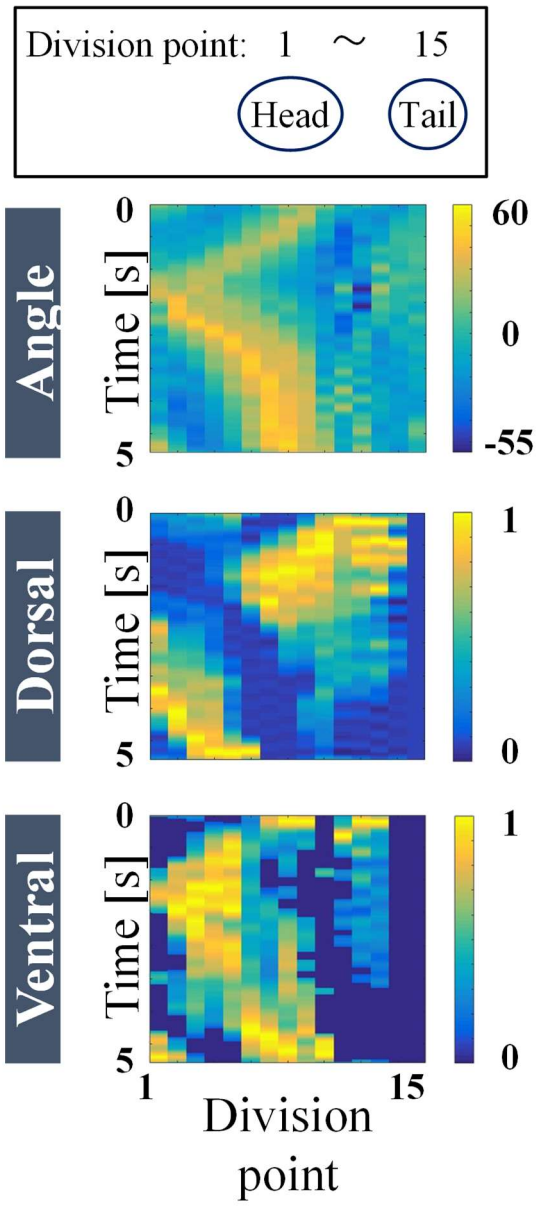

Figure 17. Color map of fluorescence rate $M_{i,l}$

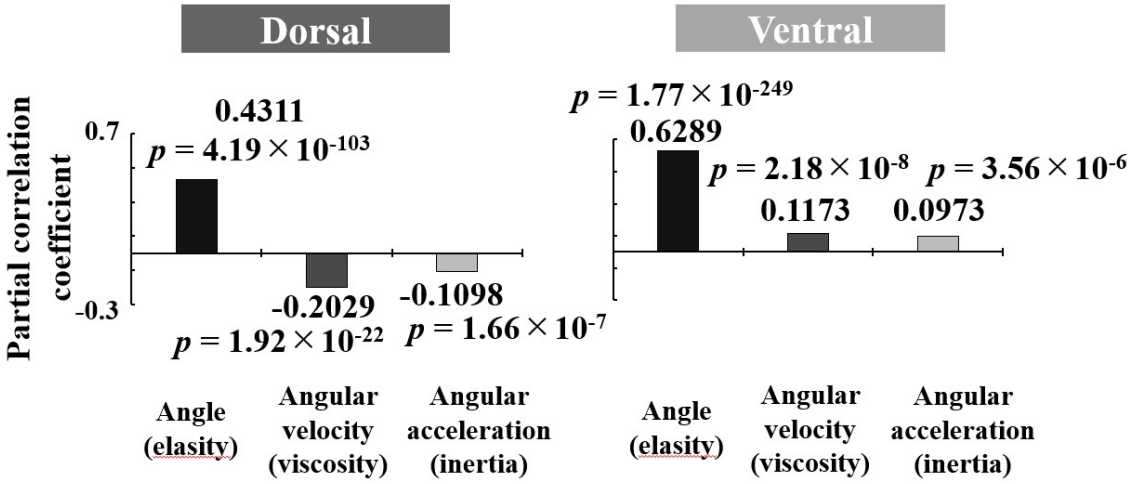

Figure 18. Partial correlation coefficients

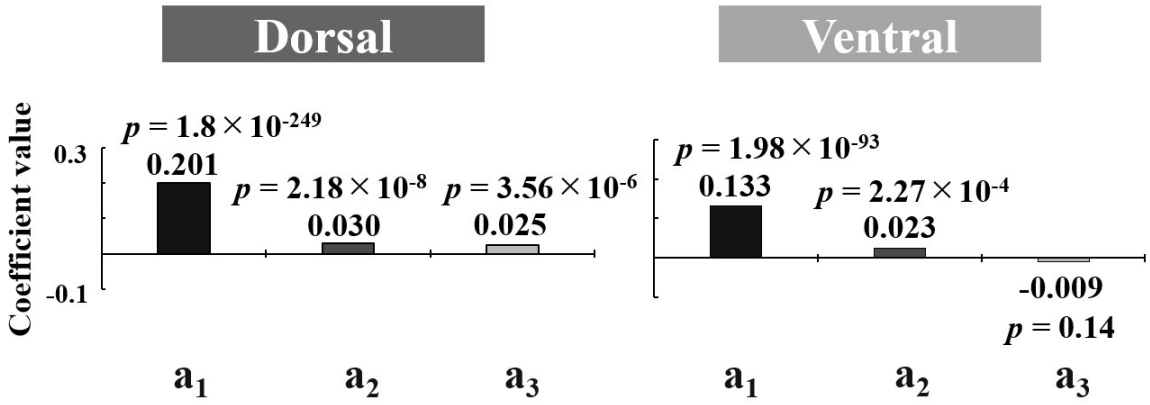

Figure 19. Coefficients of multiple regression

4.3.2 Muscle Activity Generated by the Trained Model

i. Training of model parameters

Figure 21 illustrates the convergence of the residual errors defined by the evaluation function (Eq. (38)) over ten training trials using the teacher data generated from Eqs. (39)–(41) and another ten training trials using teacher data generated from the measured muscle activity. By adjusting the model parameters, the evaluation function decreased as the learning iterations increased, and finally reached an error tolerance of $E \leq 0.005$, although the convergence speeds differ depending on the random initial parameters.

Figure 22 shows the residual errors of pre-training, post-training, and verification trials. Significant differences ($p < 0.001$) between pre-training and post-training, and pre-training and verification trials indicate that the model was successfully trained. Although significant differences were also found between the post-training and verification trials, we confirmed that the model could generate the oscillation of muscle activity and switch between oscillation patterns for forward and backward movements, as described below.

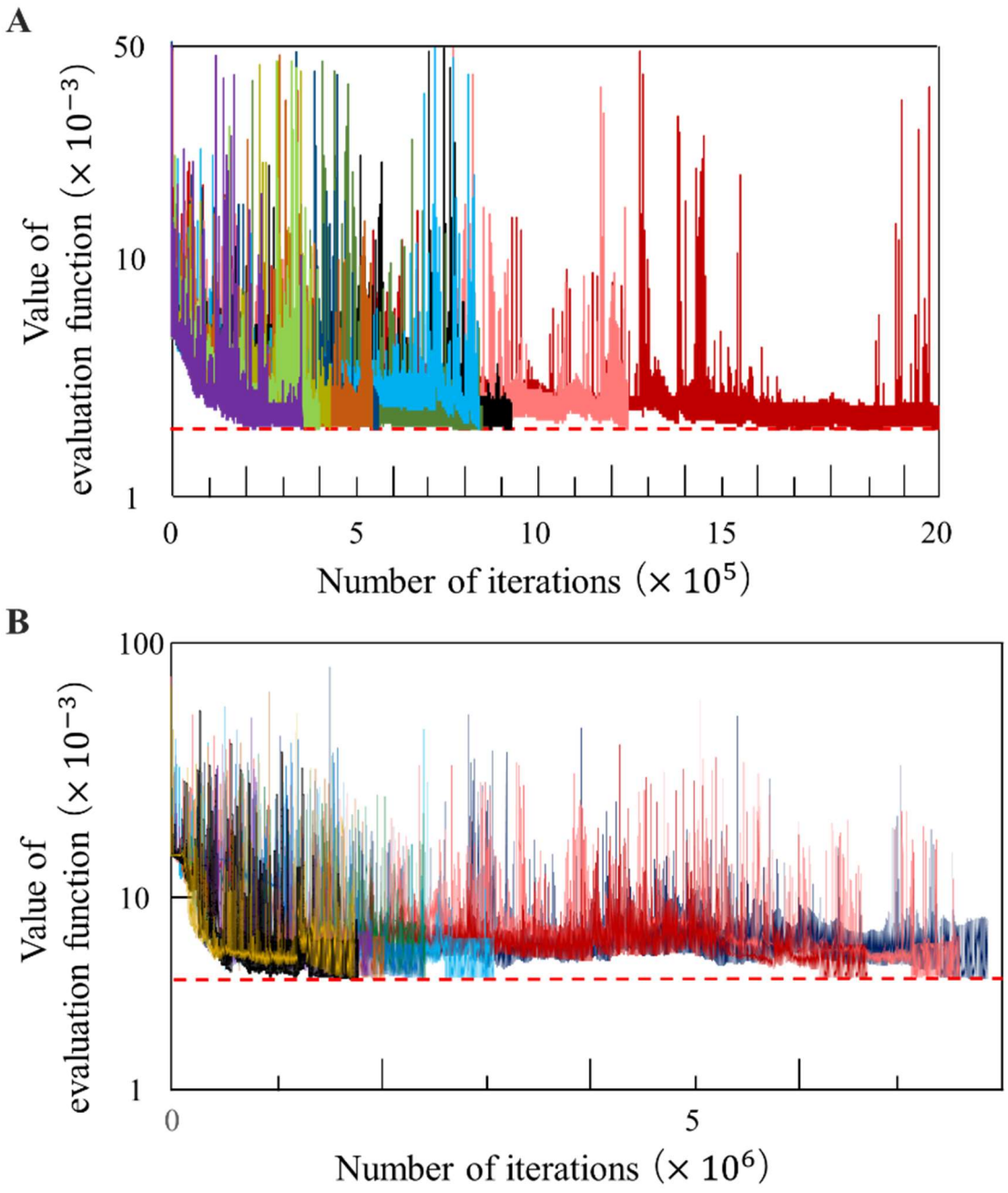

Figure 20. Learning curve.

The values of evaluation function converged through the BPTT learning algorithm for all five trials. The dotted red line represents the error tolerance. (A) Learning curve obtained from ten training trials using the teacher data generated from Eqs. (39)–(41). (B) Learning curve obtained from ten training trials using the teacher data generated from the measured muscle activity.

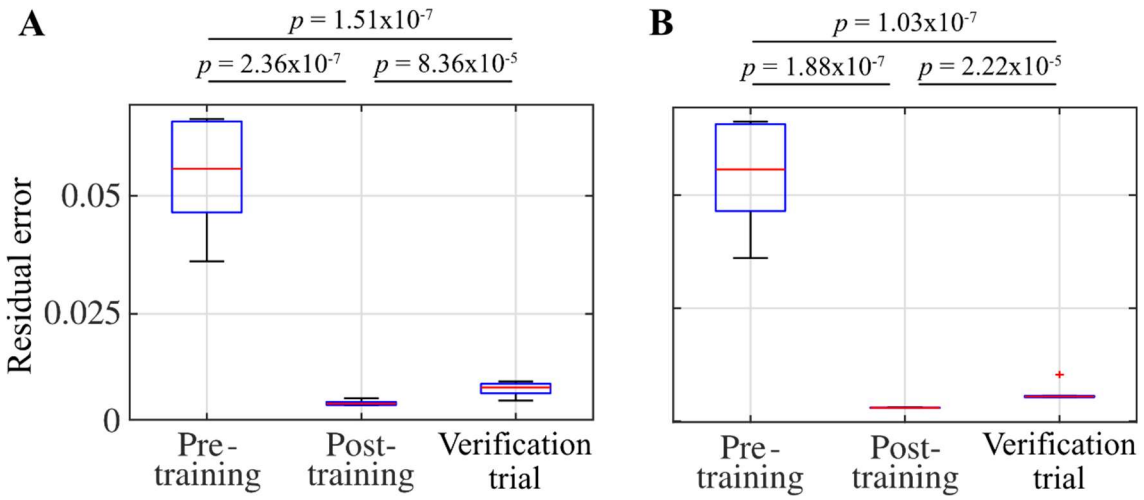

Figure 21. Residual errors.

(A) and (B) show the residual errors (see Eq. (38)) of the models trained by artificial teacher signals and measured muscle activity, respectively. Multiple comparisons with Bonferroni adjustment illustrate significant differences between the residual errors of the pre-training and post-training, and pre-training and verification trials ($p < 0.001$).

ii. Muscle activity generated by the trained model

Figure 23 shows examples of muscle activities generated by feeding trained input to the model. The two sample data shown in Fig. 23 are those with the median values of residual errors among the ten trials of training, respectively, for the two types of teacher data. The figure confirms that the muscle activity patterns corresponding to forward and backward movement are successfully generated based on the inputs from the command neurons. The muscle activity propagates from head to tail when the forward command neurons activate, and it propagates from tail to head when the backward command neurons activate. However, the model failed to generate activities in neck muscles, as shown in the output of the four–eight muscles from the head in each quadrant. This is because the model focuses on the ventral cord motor neurons and does not include the nerve ring motor neurons. The nerve ring is a neuropile involved in processing various information related to various behaviors in addition to forward and backward movement [1]. Four muscles from the head in each quadrant are innervated by the nerve ring motor neurons, and the next four muscles each in the head are innervated by both the body-wall motor neurons and head motor neurons [42]. This result indicates that the gap junctions between the muscles cannot transmit the activity pattern to the four muscles in the head, and these muscle cells are independently controlled by the nerve ring motor neurons.

In the verification simulation, we inputted command neuron signals to evoke switching between forward and backward movement at different points in time from those in the teacher data. The

switching times are $T_1 = 0.0$, $T_2 = 4.7$, $T_3 = 7.3$, $T_4 = 17.25$, $T_5 = 22.5$, and $T_6 = 28$ s for the model trained by the teacher data generated by Eqs. (39)–(41), and $T_1 = 0.0$, $T_2 = 10.1$ s for the model trained by the teacher data generated from the measured muscle activity. The outputs of the muscles are shown in Fig 24. Again, the two sample data shown in Fig 24 are those with the median values of residual errors among the ten training trials for the two types of teacher data. The results confirm that muscle activity patterns corresponding to forward and backward movement are successfully generated, as with the training data. This result indicates the generalizability of the time of switching between the forward and backward movements.

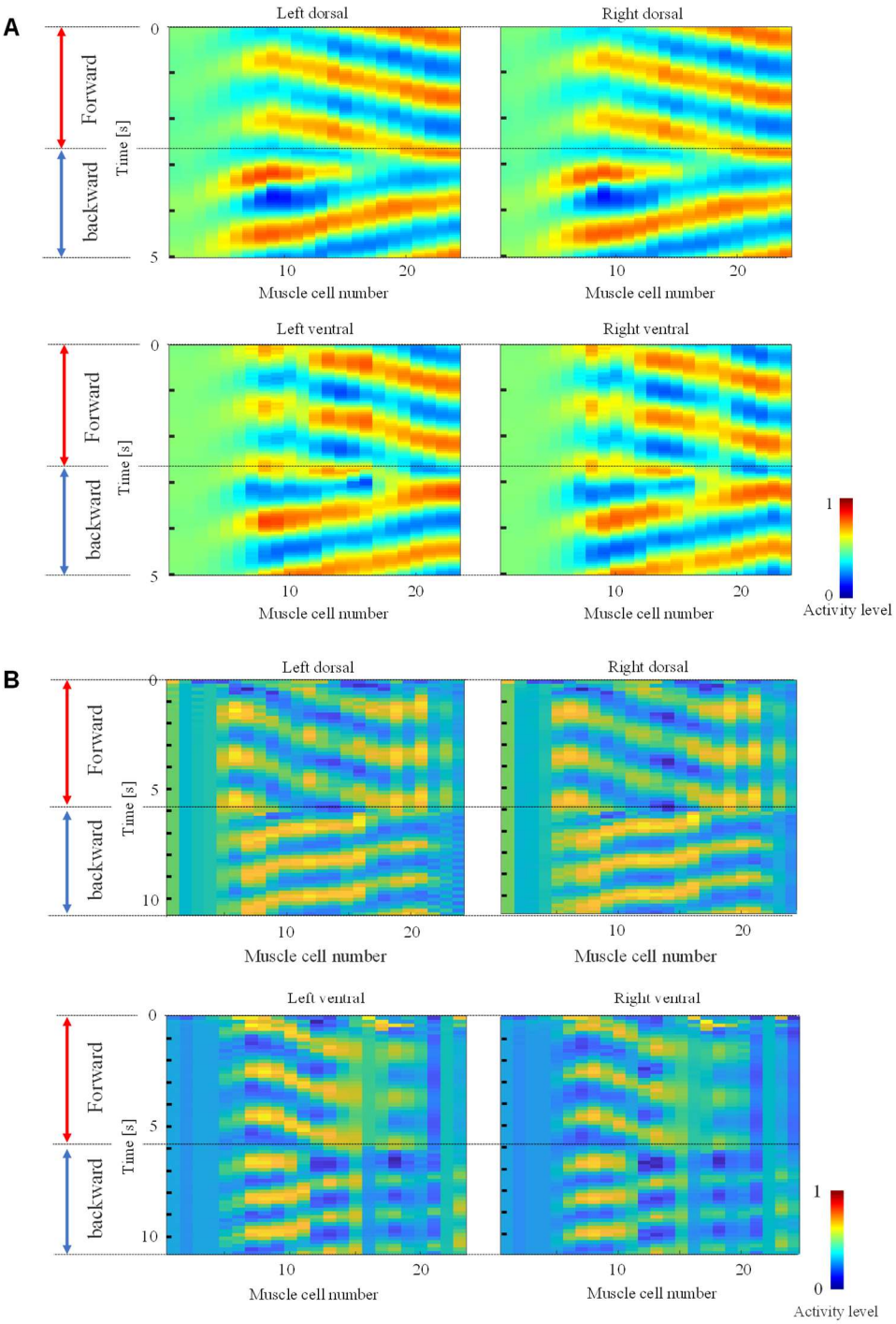

Figure 22. Muscle activities generated by the trained input.

The phases of the muscle activity are reversed as the inputs of the command neurons change. The four muscles from the head in each quadrant, controlled by the nerve ring, fail to generate oscillation patterns. In (A), the model is trained by the teacher data generated from Eqs. (39)–(41). In (B), the model is trained by the teacher data generated from the measured muscle activity.

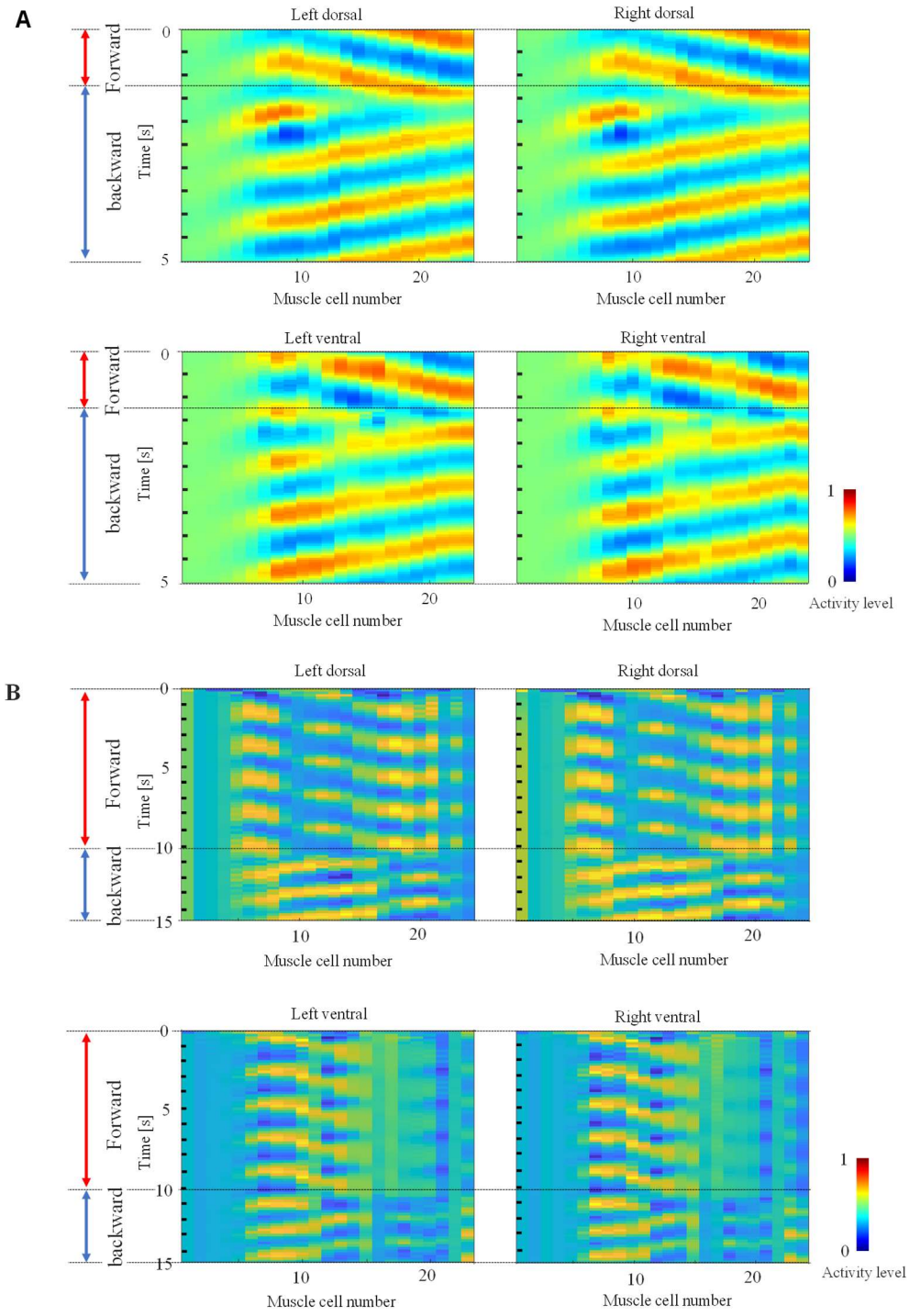

Figure 23. Muscle activities generated by the verification input.

(A) and (B) show examples of the muscle activity generated by the trained models in a verification trial, which yielded the median value of the residual errors. The activity patterns corresponding to the forward and backward movements are successfully generated by switching the phase delay, as with the training data.

4.3.3 Distribution of Synaptic and Conductance Weights

Finally, we analyzed the trained parameters, which are synaptic and conductance weights. An analysis by Snider [43] showed that the number of synapses in the actual animal follows the modified Boltzmann distribution given by the following equation:

$$p(w) = A\frac{e^{-\beta(a|w|)}}{(a|w|)^{1-\frac{1}{n}}} \quad , \tag{43}$$

where A and a are the scaling factors, β is the power index, and n is the total number of synaptic connections. We adopted this equation to fit the strength distribution of the synaptic and conductance weights. Fig 25 plots the distribution of the trained synaptic and conductance weights for each of the 10 training trials. The frequencies of weights in all training trials showed a similar trend of decreasing exponentially with the weight strength. Fig. 25 also shows the fitted line of the modified Boltzmann distribution to the mean frequency. The distribution of the trained synaptic weights and conductance weights fitted the modified Boltzmann distribution well, with coefficients of determination $R^2 = 0.972$ ($p = 1.04 \times 10^{-25}$) and $R^2 = 0.993$ ($p = 7.23 \times 10^{-17}$), respectively. This result indicates the possibility that not only the number of synapses but also the synaptic strength could follow the modified Boltzmann distribution. In addition, Fig. 25B predicts that the conductance of the gap connection could also follow the modified Boltzmann distribution.

Theoretically, synapse connections following the modified Boltzmann distribution form a candidate network structures that can maximize the information storage [43]. In this study, the neural network

model was trained to store the dynamic patterns corresponding to forward and backward motion using the BPTT algorithm, thus, as a consequence, the weights may have followed a modified Boltzmann distribution.

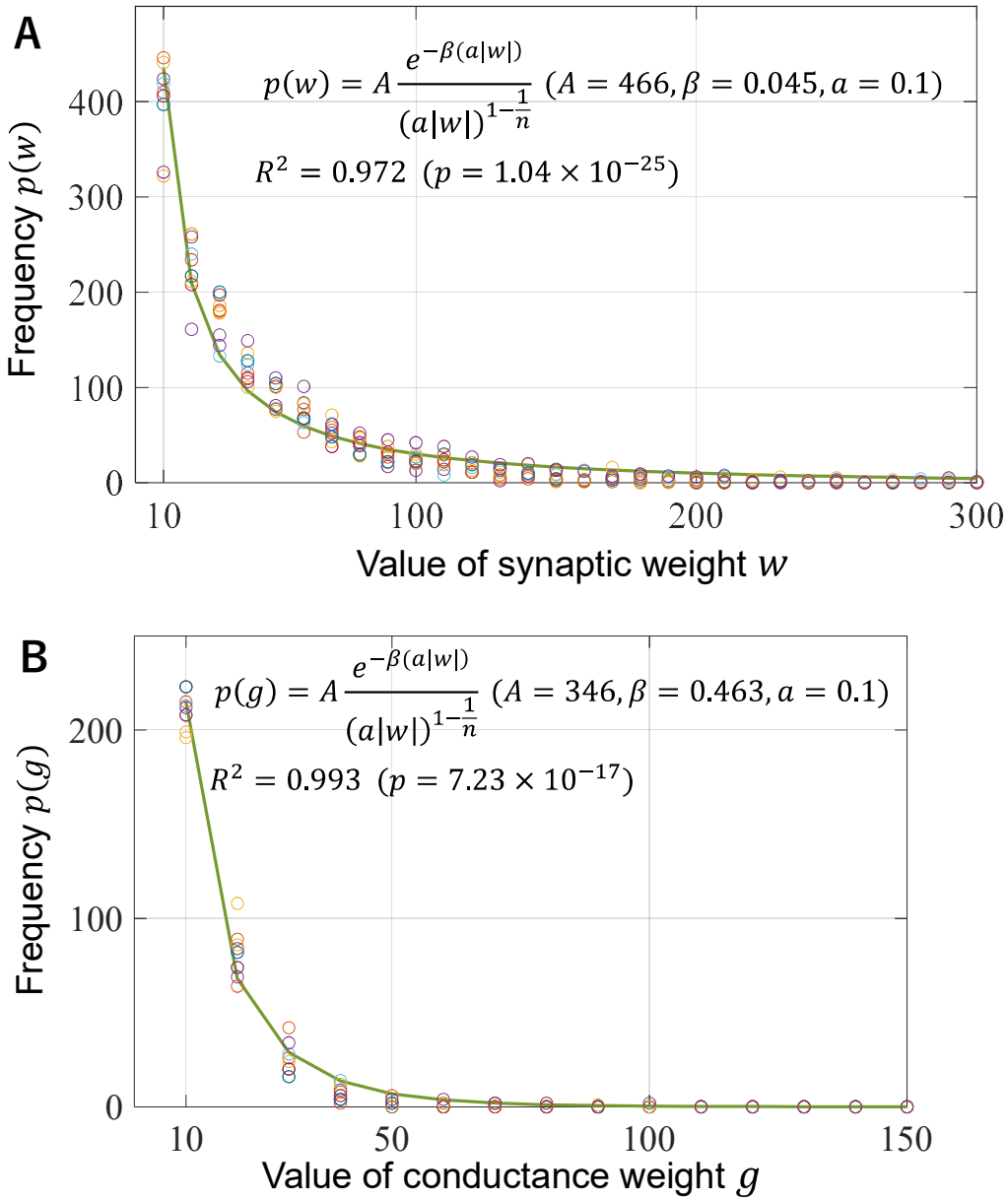

Figure 24. Distribution of weight parameters.

(A) Frequencies in the corresponding bins as a function of the synaptic weights. (B) Frequencies as a function of the conductance weights. The solid green lines represent the fit to the modified Boltzmann distribution. The distributions were obtained from 10 training trials with different initial values. The colors of the circles in the plots distinguish the different training trials.

4.4 Discussion

This study formulated a neural network model consisting of 69 motor neurons and 95 muscle cells based on the connectome of *C. elegans*. After the parameters of the model were adjusted using machine learning, it was shown that the motor neurons could generate the activity patterns of the muscle cells corresponding to forward and backward movement based on the input from the command neurons modeled as binary values. However, the four–eight muscles in the head failed to generate oscillation patterns. This result suggests that the gap junction between muscle cells cannot transmit activity to generate head motion, and the nerve ring motor neuron is necessary to control the activity of these muscles.

Previous models assigned the values of parameters by various means [16,22-27,44,45], such as manually [20] or by using an evolutional algorithm [26,44]. However, the distribution of the assigned parameter values was not analyzed. In this study, we trained the proposed model using the BPTT algorithm. We found that the modified Boltzmann distribution was well fitted to the distribution of the trained parameters (synaptic and conductance weights). This result predicts that the motor neuron and muscle network downstream of the command neurons could form a sparse network in terms of connection strength, which is advantageous to code various movement patterns [43].

While the previous models reproduced the frequency and wavelength of muscle activities, the proposed model reproduced the fluorescence rates measured from the body wall muscles using a

fluorescence strain (HBR4). Therefore, the supervised learning approach taken in this study may allow further analysis of complex activity patterns associated with movements because it provides a framework to reproduce the measured muscle activity patterns of an actual animal.

The proposed model does not consider body dynamics, which renders it unable to explore the ability of gait adaptation through proprioceptive feedback. However, these aspects of motion have already been extensively analyzed in previous models [16,22-27,44,45]. Incorporating body dynamics models [19] Gait modulation in *C. elegans*: an integrated neuromechanical model. Incorporating body dynamics models [10,22,23,27,29-31] is certainly required for the further analysis of complex movements such as an omega turn.

4.5 Conclusion Remarks

In this chapter, we presented a connectome-based neuromuscular network model of *C. elgans*. The model is trained to generate muscle oscillation patterns for both backward and forward movements using a supervised learning approach. The main finding of this study is that a motor neuron and muscle network with a sparse connection strength can generate the oscillatory patterns. In addition, the model can be trained to generate measured muscle activity patterns. Therefore, the supervised learning approach taken in this study may allow further analysis of complex activity patterns associated with movements.

Chapter 5

5 Conclusions

Chapter 2 described the neural network model of *C. elegans*. This model is composed with integrate-and-fire neuron model which the membrane potential rises sharply when the time integration of the input signal exceeds the threshold value. Imitating the information transmission method of nerve cells in an actual organism, input to each neuron is composed with term which represent information transmission by synaptic connection and term which represent information transmission by electrical connection, and neurons are connected based on construct which is clarified by biologically. The strength of the connection was optimized using Backpropagation through time (BPTT), which is a learning algorithm for recurrent neural nets.

In Chapter 3, we proposed a simple and comprehensive computational model, and derived to convert the response of a single sensory input into two types of internal representations of the NaCl gradient parallel and perpendicular to the travelling direction and enabled simultaneous simulation of the pirouette and weathervane strategies. The derived computational model suggests that internal representations of the gradients can be generated by combining head-bending angles and sensory input from ASEL/R neurons. It could also be used to interpret the functions of AIY neurons and motor neurons, respectively, identified in previous experimental[4] and simulation studies[9], and thus can bridge the gap between the chemotaxis problems at the computational and implementational levels.

The connectome-based neural network model included in the chemotaxis simulator demonstrated that the computational model could be implemented in it, although the coding manner of the chemical gradient might differ from that of the actual animals. The connectome-based neural network model may allow further analysis of the functions of respective neurons by introducing the biological constrictions and measured neural activities and by simulating ablation experiments.

In Chapter 4, we presented a connectome-based neuromuscular network model of *C. elegans*. The model is trained to generate muscle oscillation patterns for both backward and forward movements using a supervised learning approach. The main finding of this study is that a motor neuron and muscle network with a realistic weight distribution can generate the oscillatory patterns. In addition, the model can be trained to generate measured muscle activity patterns. Therefore, the supervised learning approach taken in this study may allow further analysis of complex activity patterns associated with movements.

S1 Appendix 1

Table S1 lists the symbols used in Eqs. (13) and (14).

Table S1. Symbols used in the proposed computational model

Symbol	Interpretation
$y_p,\ \dot{y}_p$	Gradient parallel to the traveling direction and its time derivative
$a_p,\ b_p$	Parameters to calculate the gradient parallel to the traveling direction
$y_w, \dot{y}_w$	Gradient perpendicular to the traveling direction and its time derivative
$a_w,\ b_w$	Parameters to calculate the gradient perpendicular to the traveling direction
q_0	Head-bending angle
$dc(\boldsymbol{x}_0, t)/dt$	Time derivative of the NaCl concentration sensed at the head tip of *C. elegans*

Table S2 lists the parameters used in the multibody model.

Table S2. Multibody model

Parameter	Value	Source
Weight	0.5 μg	[14, 15]
Length	0.10 mm	
Radius	40 μm	
Link number L	12	[23]
Normal friction[1)]	10 μN mm/s	[4]
Tangential friction[1)]	1.5 μN mm/s	

1) The friction parameters were set so that the body model travelled with an average speed of 1.2 mm/s

Table S3 shows the parameters used in the chemotaxis simulator derived from previous studies.

Table S3. Parameters used to implement pirouette and weathervane

Parameter	Value	Source
q_{Max}	0.69 rad	[22]
ω	$2\pi \times 0.80$ rad/s	
ψ	1.54 rad	[17]
C_w	1.374 rad/mM	[4]
ΔT	12 s	
C_r	0.35 rad	
T_b	6.0 s	[21]
T_{p1} [1)]	1.0 s	[4]
T_{p2} [1)]	1.18 s	
T_{p3} [1)]	1.0 s	

1) The total duration of a sharp turn is $T_{p1} + T_{p2} + T_{p3} = 3.18$ s based on [2]

S2 Appendix 2

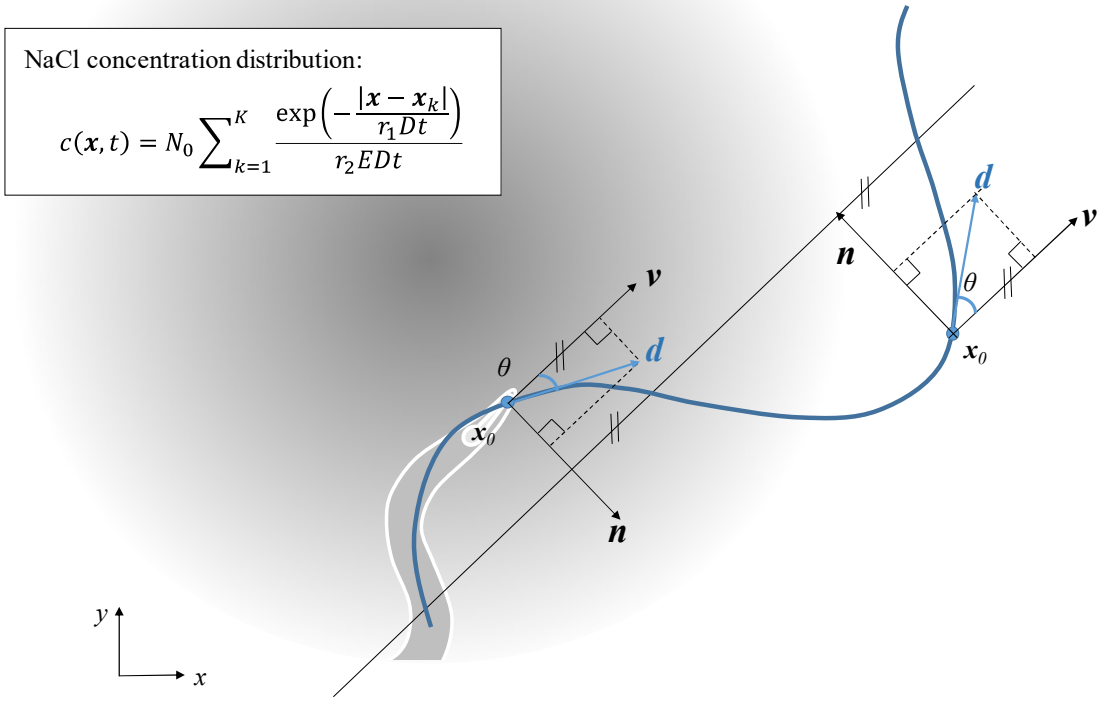

Fig S1. Definition of vectors and symbols related to head path and travelling direction: The blue line indicates the head-bending path of the animal, the black line represents the travelling direction, $\boldsymbol{x}_0=(x_0, y_0)$ is the position of the head, $\boldsymbol{v}$ is the unit vector of the travelling direction, $\boldsymbol{n}$ is the unit orthogonal vector to the travelling direction, $\boldsymbol{d}$ is the head-bending velocity vector, and θ denotes the angle between vectors $\boldsymbol{d}$ and $\boldsymbol{v}$. The circle with grey gradation represents the NaCl concentration distribution, which is expressed by the function $c(\boldsymbol{x}, t)$. The two-dimensional coordinate of the agar surface is expressed as (x, y).

This appendix shows the derivation process of the proposed computational model (equations (13) and (14)). First, based on directional decomposition, we formulate the instantaneous relationship between the NaCl concentration sensed at the nose tip and the NaCl gradients parallel and perpendicular to the traveling direction. We then take the time average of this instantaneous

relationship so that the formulation only includes the parameters accessible by the worm. Please note that we omit the explicit notation of time dependence of the variables for simplification, but all variables depend on time, unless stated otherwise. For example, the head-bending velocity vector depends on time, but we use $\boldsymbol{d}$ instead of $\boldsymbol{d}(t)$. In the following equations, we use the dot operator ($\cdot$) to express the inner product and the multiplication operator ($\times$) to express the outer product.

Step 1. Derive the instantaneous relationship between the NaCl concentration sensed at the nose tip and the NaCl gradients parallel and perpendicular to the traveling direction

The sensory neurons ASEL/R located at the nose tip respond to the time derivative of NaCl concentration, which can be expressed by the following equation:

$$\frac{dc(\boldsymbol{x}_0,t)}{dt} = \frac{\partial c(\boldsymbol{x}_0,t)}{\partial \boldsymbol{x}_0}\frac{d\boldsymbol{x}_0}{dt} + \frac{\partial c(\boldsymbol{x}_0,t)}{\partial t}$$
$$= \left[\nabla_{x,y} c(\boldsymbol{x}_0,t)\right] \cdot \boldsymbol{d} + \frac{\partial c(\boldsymbol{x}_0,t)}{\partial t}, \qquad (s2-1)$$

where the symbols are defined in the figure legend of Fig. S1. The first term of equation (s2-1) indicates the directional derivative of the NaCl distribution toward the head-bending velocity vector $\boldsymbol{d}$, and the second term indicates the temporal change in the NaCl distribution. Here, the second term can be assumed to be much smaller than the first term because the animal moves much faster than the NaCl diffuses. Thus, we can focus on the first term and approximate the time derivative of NaCl concentration given to the ASEL/R neurons by the following equation:

$$\frac{\partial c(\boldsymbol{x}_0, t)}{dt} \approx \left[\nabla_{x,y} c(\boldsymbol{x}_0, t)\right] \cdot \boldsymbol{d} \qquad (s2-2)$$

If the travelling direction $\boldsymbol{v}$ and its orthogonal vector $\boldsymbol{n}$ are given, the time derivative of NaCl concentration at the nose tip (Equation $(s2-1)$) can be decomposed into $\boldsymbol{v}$ and $\boldsymbol{n}$ direction components, which correspond to the gradients parallel and perpendicular to the travelling direction, respectively. This decomposition can be expressed by the following equations:

$$\begin{aligned} y_p \approx \tilde{y}_p &= \left\{\left[\nabla_{x,y} c(\boldsymbol{x}_0, t)\right] \cdot \boldsymbol{d}\right\}(\boldsymbol{d}/|\boldsymbol{d}| \cdot \boldsymbol{v}) \\ &= \left\{\left[\nabla_{x,y} c(\boldsymbol{x}_0, t)\right] \cdot \boldsymbol{d}\right\} \cos\theta. \qquad (s2-3) \\ y_w \approx \tilde{y}_w &= \left\{\left[\nabla_{x,y} c(\boldsymbol{x}_0, t)\right] \cdot \boldsymbol{d}\right\}(\boldsymbol{d}/|\boldsymbol{d}| \cdot \boldsymbol{n}) \\ &= \left\{\left[\nabla_{x,y} c(\boldsymbol{x}_0, t)\right] \cdot \boldsymbol{d}\right\}(\boldsymbol{d}/|\boldsymbol{d}| \times \boldsymbol{v}) \\ &= \left\{\left[\nabla_{x,y} c(\boldsymbol{x}_0, t)\right] \cdot \boldsymbol{d}\right\} \sin\theta. \qquad (s2-4) \end{aligned}$$

where $\tilde{y}_p$ and $\tilde{y}_w$ represent the approximated gradients parallel and perpendicular to the travelling direction, respectively. Equations (s2-3) and (s2-4) give the instantaneous NaCl gradients parallel and perpendicular to the traveling direction, respectively.

2. Eliminate the directional parameter θ that is not accessible by the animal

Equations (s2-3) and (s2-4) include the parameter θ, which represents the angle between the head-bending direction $\boldsymbol{d}/|\boldsymbol{d}|$ and the travelling direction $\boldsymbol{v}$, not likely accessible by the animal because the animal cannot observe the traveling direction on the global coordinates. Here, we take the time

average of equations $(s2-3)$ and $(s2-4)$ (denoted by $\bar{y}_p$ and $\bar{y}_w$, respectively) to eliminate the parameter θ:

$$\bar{y}_p = \frac{1}{t_2 - t_1}\int_{t_1}^{t_2} \tilde{y}_p \, dt = \frac{1}{t_2 - t_1}\int_{t_1}^{t_2} \left[\nabla_{x,y} c(\boldsymbol{x}_0, t)\right] \cdot \boldsymbol{d} \cos\theta \, dt$$

$$\bar{y}_w = \frac{1}{t_2 - t_1}\int_{t_1}^{t_2} \tilde{y}_w \, dt = \frac{1}{t_2 - t_1}\int_{t_1}^{t_2} \left[\nabla_{x,y} c(\boldsymbol{x}_0, t)\right] \cdot \boldsymbol{d} \sin\theta \, dt$$

Then, Steps 2.1 and 2.2 derive the NaCl gradient parallel and perpendicular to the travel direction, respectively.

Step 2.1. The gradient parallel to the traveling direction

Consider a time interval $[t_1, t_2]$ where the sign of $\cos\theta$ does not change $(-\frac{\pi}{2} \le \theta \le \frac{\pi}{2})$, and $c_{\text{low}} \le \left[\nabla_{x,y} c(\boldsymbol{x}_0, t)\right]^{\mathrm{T}} \boldsymbol{d} \le c_{\text{high}}$. The first mean value theorem for definite integrals indicates that there exist constants $c_{\text{low}} \le \tilde{\mu}_p \le c_{\text{high}}$ such that:

$$\bar{y}_p = \frac{1}{t_2 - t_1}\int_{t_1}^{t_2} \left[\nabla_{x,y} c(\boldsymbol{x}_0, t)\right] \cdot \boldsymbol{d} \cos\theta \, dt = \tilde{\mu}_p \left\{\frac{1}{t_2 - t_1}\int_{t_1}^{t_2} \cos\theta \, dt\right\}. \qquad (s2-5)$$

Because θ changes periodically, $\frac{1}{t_2 - t_1}\int_{t_1}^{t_2} \cos\theta \, dt$ becomes a constant value B_p by setting the time interval $[t_1, t_2]$ as the time duration of one θ cycle. Because θ is not accessible by the animal, we consider using the head-bending angle q_0 instead. As θ approximately synchronizes with q_0, q_0 can be expressed by same frequency parameter f as θ:

$$\theta = A_\theta \sin(2\pi f t)$$

$$q_0 = A_q \sin(2\pi f t - \psi)$$

As the time interval [t_1, t_2] is the duration of one θ cycle, the following relationship holds:

$$B_p = \frac{1}{t_2 - t_1}\int_{t_1}^{t_2} \cos\theta \, dt \approx \frac{A_p}{t_2 - t_1}\int_{t_1}^{t_2} \cos q_0 \, dt, \qquad (s2-6)$$

where A_p is a gain constant. This time average operation thus allows us to eliminate θ from Equation (s2-5), and the equation can be rewritten as follows:

$$\bar{y}_p = \frac{1}{t_2 - t_1}\int_{t_1}^{t_2} \left[\nabla_{x,y} c(\boldsymbol{x}_0, t)\right] \cdot \boldsymbol{d} \cos\theta \, dt = B_p \tilde{\mu}_p. \qquad (s2-7)$$

Here, we derive $\tilde{\mu}_p$ ($c_{\text{low}} \le \tilde{\mu}_p \le c_{\text{high}}$) by using the NaCl concentration sensed at the nose tip, approximated as $\left[\nabla_{x,y} c(\boldsymbol{x}_0, t)\right] \cdot \boldsymbol{d}$ in Equation (s2-2) by using the following leaky integration:

$$\frac{d\tilde{\mu}_p}{dt} = -a_p \tilde{\mu}_p + \tilde{b}_p \left[\nabla_{x,y} c(\boldsymbol{x}_0, t)\right] \cdot \boldsymbol{d}$$

where a_p is the reciprocal of the time constant, and $\tilde{b}_p$ is the gain constant to scale the NaCl concentration sensed at the nose tip. These parameters depend on the time duration of integration t_2-t_1 and the scale of the NaCl concentration sensed at the nose tip. Substituting the above equation into the time differentiated (s2-7) gives

$$\begin{aligned} \frac{d\bar{y}_p}{dt} &= B_p \frac{d\tilde{\mu}_p}{dt} \\ &= -a_p B_p \tilde{\mu}_p + \tilde{b}_p B_p \left[\nabla_{x,y} c(\boldsymbol{x}_0, t)\right] \cdot \boldsymbol{d} \\ &= -a_p \bar{y}_p + b_p \left[\nabla_{x,y} c(\boldsymbol{x}_0, t)\right] \cdot \boldsymbol{d} \end{aligned}$$

where $b_p = B_p \tilde{b}_p$. The gradient parallel to the travelling direction can be obtained by solving this differential equation. Then, because we approximated the time derivative of the chemical

concentration given to the sensory neurons by $\frac{dc(\boldsymbol{x}_0,t)}{dt} \approx b_p\left[\nabla_{x,y}c(\boldsymbol{x}_0,t)\right]^{\mathrm{T}}\boldsymbol{d}$, the above equation can be rewritten to Equation (13):

$$\frac{dy_p}{dt} = -a_p y_p + b_p \frac{dc(\boldsymbol{x}_0,t)}{dt} + \epsilon_p, \qquad (13)$$

where the time constant $1/a_p$ smooths the time derivative of the NaCl concentration input $dc(\boldsymbol{x}_0,t)/dt$, and the gain constant b_p scales the input. In addition, ϵ_p represents the accumulated error caused by the approximation errors in equation (*s*2-2), where the effect of NaCl diffusion is neglected, and equation (*s*2-6), where θ is replaced by q_0, and unexpected noises. This equation indicates that appropriate time averaging and scaling of the NaCl concentration sensed at the nose tip can generate the NaCl gradient parallel to the traveling direction.

Step 2.2. The gradient parallel to the traveling direction

A procedure similar to that described in step 2.1 can be used to derive equation (14) for calculating the gradient perpendicular to the travelling direction taking care of the sign of the sin function in Equation $(s2-4)$ as follows:

$$\begin{aligned}\bar{y}_w &= \frac{1}{t_2-t_1}\int_{t_1}^{t_2}\left[\nabla_{x,y}c(\boldsymbol{x}_0,t)\right]\cdot\boldsymbol{d}\sin\theta\,dt \\ &= \tilde{\mu}_w^+\left\{\frac{1}{\frac{t_2}{2}-t_1}\int_{t_1}^{\frac{t_2}{2}}\sin\theta\,dt\right\} + \tilde{\mu}_w^-\left\{\frac{1}{t_2-\frac{t_2}{2}}\int_{\frac{t_2}{2}}^{t_2}\sin\theta\,dt\right\}, \\ &= B_w(\tilde{\mu}_w^+ - \tilde{\mu}_w^-) \qquad (s2-8)\end{aligned}$$

where $\theta > 0$ in the time interval $[t_1, \frac{t_2}{2}]$, and $\theta \leq 0$ in $(\frac{t_2}{2}, t_2]$. Using the head-bending angle q_0 instead of θ gives

$$B_w = \frac{1}{\frac{t_2}{2} - t_1} \int_{t_1}^{\frac{t_2}{2}} \sin\theta \, dt = -\frac{A_w}{t_2 - \frac{t_2}{2}} \int_{\frac{t_2}{2}}^{t_2} \sin q_0 \, dt \approx \frac{A_w}{\frac{t_2}{2} - t_1} \int_{t'_1}^{\frac{t'_2}{2}} \sin q_0 \, dt, \qquad (s2-9)$$

where $q_0 > 0$ in the time interval $[t'_1, \frac{t'_2}{2}]$. The same holds for the time interval of $[\frac{t_2}{2}, t_2]$. Leaky integration for calculating $c^+_{\text{low}} \leq \mu^+_w \leq c^+_{\text{high}}$ and $c^-_{\text{low}} \leq \mu^-_w \leq c^-_{\text{high}}$ gives

$$\frac{d\mu^+_w}{dt} = -a_w \tilde{\mu}^+_w + \tilde{b}_w \left[\nabla_{x,y} c(\boldsymbol{x}_0, t)\right] \cdot \boldsymbol{d} \quad (q_0 > 0)$$

$$\frac{d\mu^-_w}{dt} = -a_w \tilde{\mu}^-_w + \tilde{b}_w \left[\nabla_{x,y} c(\boldsymbol{x}_0, t)\right] \cdot \boldsymbol{d} \quad (q_0 \leq 0)$$

Rewriting equation $(s2-4)$ gives the following equations:

$$\begin{aligned}
\frac{d\bar{y}_w}{dt} &= B_w \left(\frac{d\tilde{\mu}^+_w}{dt} - \frac{d\tilde{\mu}^-_w}{dt} \right) \\
&= \begin{cases} -B_w a_w (\tilde{\mu}^+_w - \tilde{\mu}^-_w) + B_w \tilde{b}_w \left[\nabla_{x,y} c(\boldsymbol{x}_0, t)\right] \cdot \boldsymbol{d} & (q_0 > 0) \\ -B_w a_w (\tilde{\mu}^+_w - \tilde{\mu}^-_w) - B_w \tilde{b}_w \left[\nabla_{x,y} c(\boldsymbol{x}_0, t)\right] \cdot \boldsymbol{d} & (q_0 \leq 0) \end{cases} \\
&= \begin{cases} -a_w \bar{y}_w + b_w \left[\nabla_{x,y} c(\boldsymbol{x}_0, t)\right] \cdot \boldsymbol{d} & (q_0 > 0) \\ -a_w \bar{y}_w - b_w \left[\nabla_{x,y} c(\boldsymbol{x}_0, t)\right] \cdot \boldsymbol{d} & (q_0 \leq 0) \end{cases}
\end{aligned}$$

where $b_w = B_w \tilde{b}_w$. Because $\frac{dc(\boldsymbol{x}_0, t)}{dt} \approx b_p \left[\nabla_{x,y} c(\boldsymbol{x}_0, t)\right]^{\mathrm{T}} \boldsymbol{d}$, the above equation can be rewritten as the proposed equation (14)

$$\frac{dy_w}{dt} = \begin{cases} -a_w y_w + b_w \dfrac{dc(\boldsymbol{x}_0, t)}{dt} + \epsilon_w & (q_0 > 0) \\ -a_w y_w - b_w \dfrac{dc(\boldsymbol{x}_0, t)}{dt} + \epsilon_w & (q_0 \leq 0) \end{cases} \qquad (14)$$

where $1/a_w$ is the time constant that smooths the time derivative of NaCl concentration input $dc(\boldsymbol{x}_0, t)/dt$, and b_w is the gain constant to scale the input. Further, ϵ_w represents the accumulated error caused by the approximations in equations (*s*2-2) and (*s*2-9), and unexpected noises. This

equation indicates that appropriate time averaging and scaling of the NaCl concentration sensed at the nose tip depending on the head-bending angle can generate the NaCl gradient perpendicular to the traveling direction.

S3 Appendix 3

Figure S2 shows the pirouette of the body model and the animal. In this case, the pirouette performed by the model resulted in a change in the traveling direction by approximately 162°. The figure confirms that the body model can perform pirouette in the same manner as the animal. The turning angle largely depends on the posture when the sharp turn is initiated as well as the angle between the traveling direction and the NaCl peaks, as shown in Fig. S3.

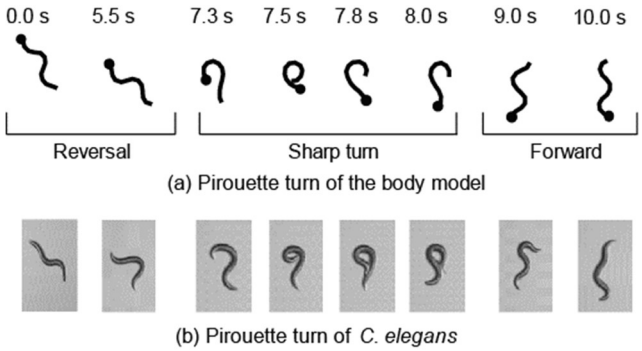

Figure S2. Body posture of *C. elegans* during a pirouette.

(a) Diagram of an example of pirouette performed by the multibody model of *C. elegans*. The reversal lasts approximately 6.0 s followed by a sharp turn lasting approximately 3.18 s, then the body model moves forward. These time parameters were derived from previous studies[2, 15]. **(b)** shows the pirouette turn performed by *C. elegans* to facilitate comparison between the movement of the multibody model and the actual worm.

Figure S3 compares the performance of weathervane and pirouette between the model and actual animal. Figure S3a shows the relationship between the spatial gradient and the average curving rate and Fig. S3b shows the distribution of bearing before the pirouette and the turning angles made by the sharp turns. Figure S3a confirmed that the weathervane index defined as the slope of the regression line is approximately 10.9, whereas that of the animal is approximately 12.0 according to the experimental data[2]. Figure S3b shows that both the simulation and animal make sharp turns with turning angles of approximately ±180° and the pirouette mostly occurs when the bearing angles are approximately ±180°.

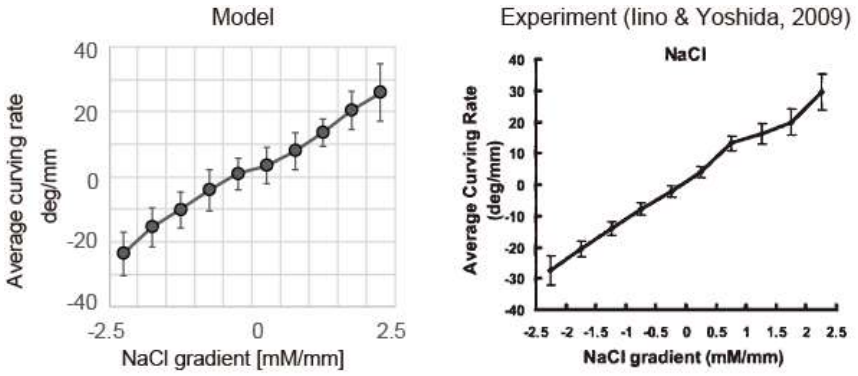

(a) The relationship between NaCl gradient and average curving rate

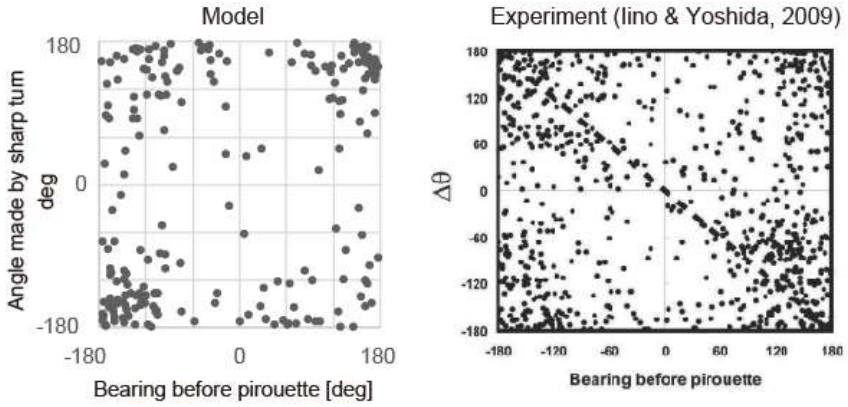

(b) The relationship between bearing of NaCl peak and angle made by sharp turn

Figure S3 Curving rate and bearing obtained from chemotaxis experiments[5] and multibody model

Graphs on the left show the simulation results and those on the right show the experimental data derived from the literature[2].

(a) Weathervane performance of the model. The *x*-axis represents the spatial gradient and the y-axis denotes the average curving rate. The error bars show the standard deviation over results of 10 simulations. On the basis of the previous study[2], the slope of the regression line was defined as the weathervane index, which was 10.9 for the simulation results and 12.0 for the animal.

(b) Pirouette performance of the model. The *x*-axis shows the bearing, which is defined as the angle between the traveling direction and the NaCl peak[2], and y-axis represents the angles between the traveling directions before and after the sharp turn.

Next, to evaluate the movement generation error caused by the multibody model, we carried out a simulation driving the multibody model by using the measured postures of the actual animal as shown in the following steps:

(1) Video-recording of the wild-type animal

The wild-type (N2) of *Caenorhabditis elegans* was maintained on the 6-cm petri plate (IWAKI

60 mm/non-treated dish; AGC Techno Glass Co., Ltd., Shizuoka, Japan) containing 10 ml of nematode growth medium (NGM) spread with overnight-incubated *Escherichia coli* OP50 (food) as previously described[S1]. An adult *C. elegans* (3.5 days) was picked up from the culture plate and washed twice with S basal buffer solution[S1]. The washed animal was placed on a 3.5-cm petri plate (IWAKI 35 mm/non-treated dish) containing 3 ml of fresh NGM without food, and the locomotion was video-recorded for 10 s or more with a digital camera video-recorder (EX-F1, Casio Computer Co., Ltd, Tokyo, Japan) mounted on a stereomicroscope (SZX16, Olympus Corporation, Tokyo, Japan) with a frame rate of 300 fps and frame size of 640 x 480 pixels.

(2) Extracting the posture of the animal

By using the video analysis software specialized for *C. elegans* (Wriggle tracker, Library Inc., Tokyo, Japan) the centroid line of the body was extracted, and fit to the multibody model with 12 links of equal length. Then, the angles between adjacent links were extracted from each video frame. Figure S4 shows the extracted angles.

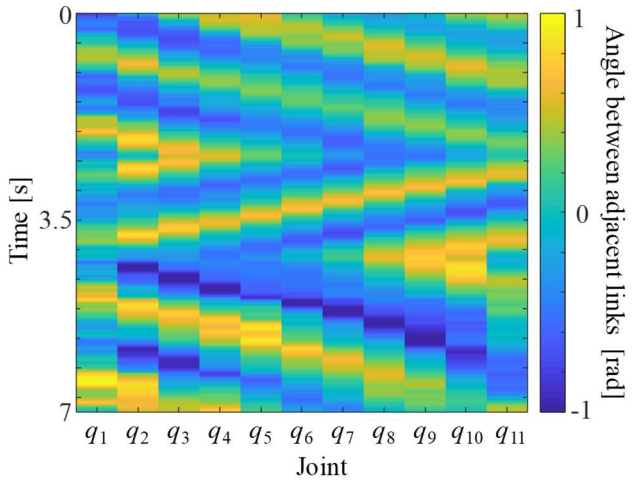

Fig. S4. Extracted angles between adjacent links. The vertical axis is time, the horizontal axis is the joint number, and the colour represents the angle corresponding to the colour bar shown on the right side. The animal showed reversal movement from around 2.5 s to 4 s, and performed an omega turn from around 4 s to 6 s.

(3) Driving the multibody model by using the extracted postures

The angles between adjacent links were substituted into the multibody model. The inverse dynamics problem was then solved to generate the traveling direction and the movement path. Figure S5 compares the paths of the multibody model and the animal.

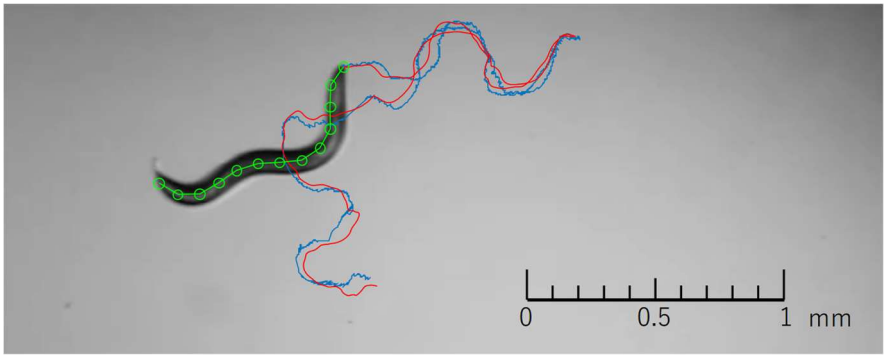

Figure S5. Comparison between the paths generated by the multibody model and the animal. The green lines with circles show the posture of the multibody model where the circles represent the joints between the adjacent links. The blue line represents the head path of the worm, and the red line represents the head path of the multibody model.

We have also attached the video file of this analysis (MultiBodyModel.avi) where the posture of the multibody model is plotted with green lines over the recorded video of the animal.

(4) Evaluating the error

Finally, we evaluated the errors between the paths. Figure S6 shows the error at each frame between the head position extracted from the video and that obtained from the multibody model. Here, the position error at each frame is normalized by the body length of the animal (approximately 1.03 mm).

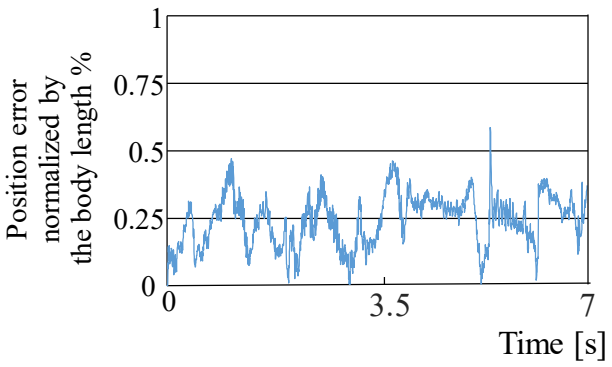

Fig. S6. Position error between the head position extracted from the video and that obtained from the multibody model. The result shows that the position error is less than 1% of body length.

This simulation result suggests that the head path error caused by the multibody model is sufficiently small.

Bibliography

[1] J. G. White, E. Southgate, J. N. Thomson, and S. Brenner, “The Structure of the Nervous System of the Nematode *Caenorhabditis elegans*,” *Philos. Trans. R. Soc. Lond. B. Biol. Sci.*, vol. 314, no. 1165, pp. 1–340, 1986, doi: 10.1098/rstb.1986.0056.

[2] J. T. Pierce-Shimomura, T. M. Morse, and S. R. Lockery, “The fundamental role of pirouettes in *Caenorhabditis elegans* chemotaxis.,” *J. Neurosci.*, vol. 19, no. 21, pp. 9557–69, Nov. 1999.

[3] Y. Iino and K. Yoshida, “Parallel use of two behavioral mechanisms for chemotaxis in *Caenorhabditis elegans.*,” *J. Neurosci.*, vol. 29, no. 17, pp. 5370–80, Apr. 2009, doi: 10.1523/JNEUROSCI.3633-08.2009.

[4] A. Kocabas, C. H. Shen, Z. V. Guo, and S. Ramanathan, “Controlling interneuron activity in Caenorhabditis elegans to evoke chemotactic behaviour,” *Nature*, vol. 490, no. 7419, pp. 273–277, 2012, doi: 10.1038/nature11431.

[5] T. C. Ferrée, B. A. Marcotte, and S. R. Lockery, “Neural network models of chemotaxis in the nematode *Caenorhabditis elegans*,” *Adv. Neural Inf. Process. Syst.*, pp. 55–61, 1997.

[6] T. C. Ferrée and S. R. Lockery, “Computational rules for chemotaxis in the nematode *C. elegans*,” *J. Comput. Neurosci.*, vol. 6, no. 3, pp. 263–277, 1999, doi: 10.1023/A:1008857906763.

[7] T. Morse, S. Lockery, and T. Ferrée, “Robust spatial navigation in a robot inspired by chemotaxis in *Caenorhabditis elegans*,” *Adapt. Behav.*, vol. 6, no. 3–4, pp. 393–410, 1998.

[8] E. J. Izquierdo and S. R. Lockery, “Evolution and analysis of minimal neural circuits for klinotaxis in *Caenorhabditis elegans.*,” *J. Neurosci.*, vol. 30, no. 39, pp. 12908–17, Sep. 2010, doi: 10.1523/JNEUROSCI.2606-10.2010.

[9] E. J. Izquierdo and R. D. Beer, “Connecting a Connectome to Behavior: An Ensemble of Neuroanatomical Models of *C. elegans* Klinotaxis,” *PLoS Comput. Biol.*, vol. 9, no. 2, 2013, doi: 10.1371/journal.pcbi.1002890.

[10] X. Deng, J.-X. Xu, J. Wang, G. Wang, and Q. Chen, “Biological modeling the undulatory locomotion of *C. elegans* using dynamic neural network approach,” *Neurocomputing*, pp. 1–11, 2016, doi: 10.1016/j.neucom.2015.12.090.

[11] H. Suzuki, R. Kerr, and L. Bianchi, “In vivo imaging of *C. elegans* mechanosensory neurons demonstrates a specific role for the MEC-4 channel in the process of gentle touch sensation,” *Neuron*, vol. 39, pp. 1005–1017, 2003.

[12] M. Chalfie, J. E. Sulston, J. G. White, E. Southgate, J. N. Thomson, and S. Brenner, “The neural circuit for touch sensitivity in *Caenorhabditis elegans.,*” *J. Neurosci.*, vol. 5, no. 4, pp. 956–64, 1985, doi: 3981252.

[13] E. Niebur and P. Erdös, “Theory of the locomotion of nematodes: control of the somatic motor neurons by interneurons.,” *Math. Biosci.*, vol. 118, no. 1, pp. 51–82, Nov. 1993.

[14] J. M. Gray, J. J. Hill, and C. I. Bargmann, “A circuit for navigation in *Caenorhabditis elegans.,*”

Proc. Natl. Acad. Sci. U. S. A., vol. 102, no. 9, pp. 3184–91, 2005, doi: 10.1073/pnas.0409009101.

[15] P. J. Werbos, "Generalization of backpropagation with application to a recurrent gas market model," *Neural Networks*, vol. 1, no. 4, pp. 339–356, 1988, doi: 10.1016/0893-6080(88)90007-X.

[16] J. Karbowski, G. Schindelman, C. J. Cronin, A. Seah, and P. W. Sternberg, "Systems level circuit model of *C. elegans* undulatory locomotion: Mathematical modeling and molecular genetics," *J. Comput. Neurosci.*, vol. 24, no. 3, pp. 253–276, 2008, doi: 10.1007/s10827-007-0054-6.

[17] A. O. W. Stretton, R. M. Fishpool, E. Southgate, J. E. Donmoyer, J. P. Walrond, and I. S. Kass, "Structure and physiological activity of the motorneurons of the nematode Ascaris," *Proc. Natl. Acad. Sci. USA*, vol. 75, no. 7, pp. 3493–3497, 1978, doi: 10.1073/pnas.75.7.3493.

[18] S. Kato *et al.*, "Global Brain Dynamics Embed the Motor Command Sequence of *Caenorhabditis elegans*," *Cell*, vol. 163, no. 3, pp. 656–669, 2015, doi: 10.1016/j.cell.2015.09.034.

[19] J. Ben Arous, Y. Tanizawa, I. Rabinowitch, D. Chatenay, and W. R. Schafer, "Automated imaging of neuronal activity in freely behaving *Caenorhabditis elegans*," *J. Neurosci. Methods*, vol. 187, no. 2, pp. 229–234, 2010, doi: 10.1016/j.jneumeth.2010.01.011.

[20] S. Faumont *et al.*, "An Image-Free Opto-Mechanical System for Creating Virtual Environments and Imaging Neuronal Activity in Freely Moving *Caenorhabditis elegans,*" *PLoS One*, vol. 6, no. 9, p. e24666, 2011, doi: 10.1371/journal.pone.0024666.

[21] Q. Wen *et al.*, "Proprioceptive Coupling within Motor Neurons Drives *C. elegans* Forward

Locomotion," *Neuron*, 2012, doi: 10.1016/j.neuron.2012.08.039.

[22] J. H. Boyle, S. Berri, and N. Cohen, "Gait modulation in *C . elegans*: an integrated neuromechanical model," *Front. Comput. Neurosci.*, vol. 6, no. March, pp. 1–15, 2012, doi: 10.3389/fncom.2012.00010.

[23] J. E. Denham, T. Ranner, and N. Cohen, "Intrinsic and Extrinsic Modulation of *C. elegans* Locomotion," *bioRxiv*, vol. 20, pp. 1–7, 2018, doi: 10.1101/312132.

[24] C. Fieseler, J. Kunert-Graf, and J. N. Kutz, "The control structure of the nematode *Caenorhabditis elegans*: Neuro-sensory integration and proprioceptive feedback," *J. Biomech.*, vol. 74, pp. 1–8, 2018, doi: 10.1016/j.jbiomech.2018.03.046.

[25] J. Kunert, E. Shlizerman, and J. N. Kutz, "Low-dimensional functionality of complex network dynamics: Neurosensory integration in the *Caenorhabditis elegans* connectome," *Phys. Rev. E - Stat. Nonlinear, Soft Matter Phys.*, vol. 89, no. 5, pp. 1–6, 2014, doi: 10.1103/PhysRevE.89.052805.

[26] E. J. Izquierdo and R. D. Beer, "An Integrated Neuromechanical Model of Steering in *C. elegans*," pp. 199–206, 2015, doi: 10.7551/978-0-262-33027-5-ch040.

[27] P. Gleeson, D. Lung, R. Grosu, R. Hasani, and S. D. Larson, "C302: A multiscale framework for modelling the nervous system of *Caenorhabditis elegans*," *Philos. Trans. R. Soc. B Biol. Sci.*, vol. 373, no. 1758, 2018, doi: 10.1098/rstb.2017.0379.

[28] J. Bryden and N. Cohen, "Neural control of *Caenorhabditis elegans* forward locomotion: The role

of sensory feedback," *Biol. Cybern.*, vol. 98, no. 4, pp. 339–351, 2008, doi: 10.1007/s00422-008-0212-6.

[29] M. Suzuki, T. Tsuji, and H. Ohtake, "A model of motor control of the nematode *C. elegans* with neuronal circuits," *Artif. Intell. Med.*, vol. 35, no. 1–2, pp. 75–86, 2005, doi: 10.1016/j.artmed.2005.01.008.

[30] A. Palyanov, S. Khayrulin, and S. D. Larson, "Three-dimensional simulation of the *Caenorhabditis elegans* body and muscle cells in liquid and gel environments for behavioural analysis," *Philos. Trans. R. Soc. B Biol. Sci.*, vol. 373, no. 1758, 2018, doi: 10.1098/rstb.2017.0376.

[31] Z. Soh, K. Sakamoto, M. Suzuki, Y. Iino, and T. Tsuji, "A computational model of internal representations of chemical gradients in environments for chemotaxis of *Caenorhabditis elegans*.," *Sci. Rep.*, vol. 8, no. 1, p. 17190, 2018, doi: 10.1038/s41598-018-35157-1.

[32] Xu, J. X., Deng, X. & Ji, D. "Study on *C. elegans* behaviors using recurrent neural network model," in *2010 IEEE Conference on Cybernetics and Intelligent Systems.* 1–6 (IEEE, 2010). doi: 10.1109/ICCIS.2010.5518591

[33] Marr, D. & Poggio, T. "From understanding computation to understanding neural circuitry," *Neurosci. Res. Program. Bull.*, **15,** 470–488 (1977).

[34] WormAtlas, Altun, Z.F., Herndon, L.A., Wolkow, C.A., Crocker, C., Lints, R. and Hall, D.H. (ed.s) 2002-2020. http://www.wormatlas.org

[35] Bryden J, Cohen N. "Neural control of *Caenorhabditis elegans* forward locomotion: The role of sensory feedback," Biol Cybern. 2008;98(4): 339–351.

[36] White, J. "The Anatomy in *The nematode C. elegans*," (ed. Wood, W. B.), Chapter 4, 81–122 (Cold Spring Harbor Laboratory Press, 1988).

[37] Sakata, K. & Sihingai, R. "Neural network model to generate head swing in locomotion of *Caenorhabditis elegans*," *Network: Comput. Neural Syst.* **15,** 199–216 (2004).

[38] Schwarz, J, Spies, J-P & Bringmann, H., "Reduced muscle contraction and a relaxed posture during sleep-like Lethargus," *Worm* **1(1)**, 12-14 (2012)

[39] X. N. Shen, J. Sznitman, P. Krajacic, T. Lamitina and P. E. Arratia, "Undulatory locomotion of *Caenorhabditis elegans* on wet surfaces," Biophysical Journal, Vol. 102, pp. 2772–2781, 2012.

[40] Chronis N, Zimmer M, Bargmann CI, Microfluidics for in vivo imaging of neuronal and behavioral activity in *Caenorhabditis elegans*, Nat Methods. 2007;4: 727–731.

[41] Suzuki M, Sakashita T & Funayama T. Immobilization of live *Caenorhabditis elegans* individuals using an ultra-thin polydimethylsiloxane microfluidic chip with water retention. J. Vis. Exp. 145, e59008 (2019).

[42] Ware RW, Clark D, Crossland K, Russell RL. "The nerve ring of the nematode *Caenorhabditis elegans*: Sensory input and motor output," J Comp Neurol. 1975;162(1): 71–110.

[43] Snider J. "Indistinguishable synapses lead to sparse networks," Neural Comput. 2018;30: 708–722. doi:10.1162/neco_a_01052

[44] Olivares EO, Izquierdo EJ, Beer RD. "Potential role of a ventral nerve cord central pattern generator in forward and backward locomotion in *Caenorhabditis elegans*," Netw Neurosci. 2018;2: 323–343. doi:10.1162/netn_a_00036

[45] Mailler R, Avery J, Graves J, Willy N. "A biologically accurate 3D model of the locomotion of *Caenorhabditis elegans*," 2010 Int Conf Biosci 2010. 2010;84–90. doi:10.1109/BioSciencesWorld.2010.18

Acknowledgments

I wish to thank my advisor, Professor Toshio Tsuji, for his advice, suggestions, encouragement and patience. He has taught me in the various research fields of biosignal analysis, machine learning, neural networks, and human–machine interfaces. His serious attitude for research has been an excellent example to me.

I would like to acknowledge committee members Professor Idaku Ishii and Professor Toru Yamamoto for their invaluable suggestions and discussions on this dissertation. Many thanks also go to Professor Yuichi Kurita, Professor Zu Soh, Ms. Michiyo Suzuki, and Professor Akira Furui for their helpful comments and kind efforts to support my research, my spirit, and my daily life.

I must also take this opportunity to acknowledge Mr. Yusuke Kishishita, Mr. Shinya Nishikawa, Mr. Hiroki Yamashita, and all the members of the Biological Systems Engineering Laboratory at Hiroshima University for their encouragement and support.

Finally, my deepest gratitude goes to my family for supporting my life. I was able to finish writing this thesis because of their support. Again, special thanks goes to my family.